Ceramic-metal (cermet) composites: A review of key properties and synthesis methods focused on nuclear waste immobilization

Jonathan S. Evarts[a,b], Saehwa Chong[a], Jared M. Oshiro[a], Brian J. Riley[a], R. Matthew Asmussen[a], John S. McCloy[a,b]

[a] *Pacific Northwest National Laboratory, Richland, WA 99354, USA*

[b] *School of Mechanical and Materials Engineering, Washington State University, Pullman, WA 99164, USA*

keywords: ceramic-metal composites; metal matrix composites; cermet; hard metals; salt waste forms; nuclear waste immobilization; radioactive waste

Abstract

This paper reviews key properties, applications, and examples of ceramic-metal composites (cermets), and metal matrix composites (MMC) with emphasis on their applicability as waste forms for immobilizing nuclear waste. While the literature is mature for vitrified and cementitious radioactive waste forms, cermet materials have not received adequate attention as potential candidates for immobilizing nuclear waste. To promulgate this effort, this review connects cermet and MMC design, such as hardened tools, with the chemistry of radioactive waste streams. A discussion on certification and qualification standards for cermet waste forms, literature gaps, and "how-to" sections on cermet processing techniques. Key parameters discussed include thermal conductivity, chemical durability, and waste loading, as well as examples for metal-containing waste forms. As cermet waste forms gain momentum within the community, this review paper aims ensure the end-of-life nuclear fuel cycle is addressed from a materials and waste disposition perspective.

1 Introduction

Ceramic-metal (cermet) composite materials have uses across multiple domains including industrial tooling,[1,2] nuclear thermal propulsion,[3,4] and radioactive waste forms.[5-8] It is useful to note in literature, terms such as cermets, metal matrix composites (MMC), ceramic matrix composites (CMC), and hard-metals generally imply a material consisting of a mixture of a ceramic and metal phase; however, in cermets, the ceramic phase has a larger volume fraction, which is bonded by a metallic phase to improve toughness or thermal conductivity of the material.[9] This differentiates cermets from MMCs and CMCs where a ceramic is added as a reinforcement phase.[9] Hereafter, having similar processing methods, MMCs and cermets are discussed, due to favorable properties which would benefit a radioactive material waste form. The first reported patent in this field was issued to a German company "Osram Studiengesellschaft" in 1923.[10] Since this time, cermets have rapidly evolved, especially in the tool industry where high hardness, toughness, and thermal conductivity are desirable properties.[1,2]

Although much research has been accomplished on cermets, few studies have investigated the feasibility of using cermets as radioactive waste forms. Aaron et al.[5] first proposed the use of cermets as a

radioactive waste form in 1979 due to potential high waste loading, high thermal conductivity, good leach resistance, high durability and mechanical strength, and low losses of volatile radioisotopes during processing. In 2011, to lower internal thermal stresses in radioactive waste forms, Ortega et al.[6] rekindled the interest in cermets for immobilizing cesium and strontium from aqueous waste streams generated from reprocessing spent nuclear fuel (SNF). This was subsequently generalized to high-heat producing radioisotopes generated in the nuclear fuel cycle.[7] The purposes of this review are to provide examples of where cermets have been documented in the scientific literature, to inform the community of the advantages and disadvantages of cermets as radioactive waste forms, to summarize key properties of interest when designing cermets, and to provide an overview of the options for fabricating cermets and research that should be conducted to support this effort.

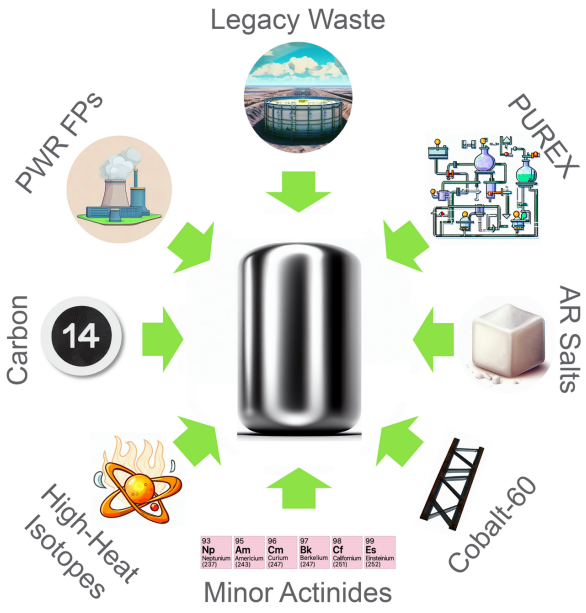

Figure 1. Infographic demonstrating the potential waste streams that can be incorporated into a cermet waste form, and the flexibility in composition for radioisotope immobilization. Examples above include waste from legacy defense processes, PUREX process, advanced reactor molten salts, activated structural materials, minor actinides, high-heat producing isotopes such as ^{137}Cs and ^{90}Sr, radioactive carbon, and fission products from pressurized water reactors.

2 Waste Streams

As depicted in Figure 1, radioactive waste is generated from a diverse set of sources including commercial nuclear power production, legacy (defense) waste processing, research activities, nuclear

accidents, and medical isotope production.[11] A brief discussion on types of waste streams from nuclear legacy waste, light water reactors (LWR), and advanced reactors (AR) is presented here. For an in-depth review, the reader is referred to the references herein.

2.1 Legacy Waste

Legacy waste includes military waste streams from the Hanford plutonium production reactors, which produced waste with high concentrations of fission products, including halides.[12,13] In vitrified waste forms, such as borosilicate glass, the solubility of halides is very low and this limits overall waste loading.[14-16] While this is true, it is expected that halides and other volatiles with low solubility in the glass melt will report to the off-gas system. Additionally, halides such as chlorine, iodine, and bromine, have very high mobilities in oxidizing environments.[17] Defense wastes from weapons production, including the bismuth phosphate process, the reduction-oxidization (REDOX) process, and the plutonium uranium reduction extraction (PUREX) process at the Hanford site have been well documented.[18-20] Hanford site waste tanks have highly variable compositions, but generally the major constituents are sodium, nitrates, nitrites, carbonates, aluminum, phosphate, and sulfates, with minor species of bismuth, silicon, uranium, zirconium, chromium, and oxalate.[20,21]

2.2 Light Water Reactors Reprocessing Raffinate

In an open-nuclear fuel cycle, LWRs produce a variety of isotopes that require immobilization and disposition. In the United States, as a result of the Carter administration policy, the current waste management strategy for SNF from LWRs is at-reactor storage for decay of fission products until a high-level waste repository is identified where it could eventually be directly disposed. Typical SNF contains 95% ^{238}U, 3% fission products, 1% plutonium, and 1% ^{235}U (by mass).[17] Table 1 provides a summary of some common fission products found in SNF. In a closed-nuclear fuel cycle, the LWR spent nuclear fuel is reprocessed to recover the unused uranium fuel. The PUREX and the Advanced PUREX process are standard reprocessing method where the zircalloy cladding is removed, and the fuel is dissolved in nitric acid. This process generates an aqueous waste stream that can be calcined forming a multitude of oxides

distributed around half the atomic weight of uranium.[12] The LWR waste streams, such as the calcined metal oxides of fission products and calcined oxides, could be immobilized within a cermet waste form.

Table 1. Common fission products found in a LWR SNF (mol%) including the half-life ($t_{1/2}$; in years unless otherwise noted). This table was reproduced with permission from.[22] Copyright Elsevier 2019.

Short-Lived			Long-Lived		
Radionuclide	Content	$t_{1/2}$ (y)	Radionuclide	Content	$t_{1/2}$ (y)
^{106}Ru, ^{106}Rh	0.51	1.02, 29.9 s	^{79}Se	0.01	6.5×10^{4}
^{125}Sb	0.022	2.758	^{93}Zr	2.7	1.53×10^{6}
^{134}Cs	0.47	2.065	^{99}Tc	2.9	2.13×10^{5}
^{147}Pm	0.25	2.62	^{107}Pd	0.74	6.50×10^{6}
^{154}Eu	0.1	8.59	^{126}Sn	0.05	2.18×10^{5}
^{155}Eu	0.013	4.71	^{129}I	0.61	1.57×10^{7}
^{85}Kr	0.11	10.73	^{135}Cs	0.81	2.3×10^{6}
^{90}Sr	2	29.1	^{166m}Ho	10^{-6}	1.2×10^{3}
^{137}Cs	3	30.17			

2.3 Advanced Reactors

To meet the increasing demand for energy, governments and private companies are developing novel reactor concepts, which will generate waste streams quite different than those of legacy or LWR wastes. The Generation IV International Forum (GIF) has down-selected six reactor technologies for advancement: Molten Salt Reactor (MSR), Gas-Cooled Fast Reactor (GFR), Supercritical Water-cooled Reactor (SWCR), Lead-cooled Fast Reactor (LFR), Very High Temperature Reactor (VHTR), and Sodium-cooled Fast Reactor (SFR). Potential wastes from MSRs requiring immobilization include particulates, aerosols, reactive gases such as $^{3}H_{(g)}$ and $^{3}H_2O$, residual halides, noble gases, and oxygen and nitrogen isotopes.[23] Table S1 (Supporting Information)[24-39] lists several strategies for immobilization; however, several of the waste streams coming out of these reactor concepts could be processed and immobilized within a cermet waste form, such as metallic streams (e.g., reactor containment, heat exchangers, transfer lines, pumps), ceramic streams (e.g., silicon carbide), salt streams (e.g., molten salt reactor fuels/coolants), and off-gas byproducts.[23]

Fast reactors (FR)s, such as GFRs, LFRs, and SFRs, are a unique type of nuclear reactor where the minor actinides are recycled through a partitioning and transmutation process.[40] This process physically and/or chemically separates fission products, actinides, and other valuable isotopes from the waste stream. From a waste management perspective, isotopes of concern may be recycled back into an AR where they are irradiated with fast neutrons to transform them into shorter-lived or stable isotopes.[41] While a fully closed fuel cycle can reduce high-level waste volume by *ca.* 30%, the processes required for iterative recycling generates new waste streams to be treated for disposal.[41-44] Table S2 (Supporting Information) illustrates the mass flow of heavy metals, fuel compositions at equilibrium that must be considered in various reactors, and spent fuel processing scenarios following the fuel cooling phase.[41]

It is also valuable to note that FRs incur only modest gains in short-term (< 50 yrs) decay heat reduction; however at 200 years, a 20–30 fold reduction in heat generation can be achieved.[41] For a vitrified waste form, heat generation may delay vitrification until sufficient cooling is achieved to maintain glass in a solid state; this delayed cooling could cause the waste form to flow and even devitrify (crystallize or phase separate).[41,45] However, in a cermet waste form, a waste cooling period may be unwarranted if the phases remain stable at temperature and/or the thermal conductivity is sufficiently high. In a fully closed cycle, ^{137}Cs and ^{90}Sr cannot be transmuted and thus are the primary short-lived heat-producing radioisotopes when disposing of high-level waste from these processes.[40] Concerning radiotoxicity, minor actinides ^{237}Np ($t_{1/2}$ = 2.14 × 10^6 y), ^{243}Am ($t_{1/2}$ = 7,364 y), ^{245}Cm ($t_{1/2}$ = 8,423 y), and ^{246}Cm ($t_{1/2}$ = 4,706 y) are the primary radioisotopes of concern for fuel irradiated in FRs, due to their long half-lives.[40,41]

Given the examples of waste streams from legacy defense waste, LWRs and ARs, and the limitations of the current borosilicate glass waste form technology, the need for a new versatile waste form process to treat and immobilize a wide range of waste streams is evident. Additionally, there exist a significant number of options for metallic binder materials and reinforcement phases. Mussatto et al.[46] reviewed 944 MMC papers, and found that there have been 80 different metal matrix materials and 294 different reinforcement phases studied. Moreover, employing a waste form with customizable properties to

accommodate both legacy and prospective wastes would offer considerable benefits. Hereafter, the use of cermets to immobilize radioisotopes from the aforementioned waste streams is discussed.

3 Fabrication for Cermets and MMCs

Multiple fabrication methods exist to produce cermets and MMCs. Typical methods include both solid state methods, such as powder metallurgy, and liquid state methods, such as centrifugal casting, stir casting, , and in-situ methods.[47] These methods have been successfully employed on a variety of matrix and dispersed materials.[47-51]

Figure 2 proposes some composite relationships and nomenclature for waste forms containing multiple phases including binary and ternary systems. Figure 2a provides information for a basic cermet waste form containing a maximum of two separate phases, e.g., metal-encapsulated iodosodalite[52]. Figure 2b provides an overview of what the system might look like if a third phase were present such as a halide phase. Examples of halide-containing nuclear waste streams include: MSR salt streams,[23] electrorefiner salts from electrochemical reprocessing,[53] iodine-containing streams from caustic scrubbers,[54] or radioiodine-loaded solid sorbents.[31,54,55] An example of this cermet might be a waste form fabrication with an AgI-containing ceramic phase, such as iodine-loaded silver mordenite (AgZ) within a metallic encapsulant matrix whereby the metal used (e.g., Bi^0, Sn^0, Pb^0) could form stable metal-iodide compounds if it were to be released from the AgI (e.g., Bi_5O_7I, BiOI, SnI_4, PbI_2).[56,57] Similar work was done by Bruffey et al.[58-60], Jubin et al.[61], and Maddrell et al.[62] whereby iodine-loaded AgZ was consolidated using hot isostatic pressing (HIPing), where the hot isostatic press (HIP) canister itself is basically a metallic encapsulant phase. Although the final product is not considered a cermet here, this example provides insight into the idea of encapsulation. Figure 2c provides a concept whereby multiple metal phases are included in the waste form process. This could be done by encapsulating a standard cermet in a metal HIP container and/or by including a multi-layered HIP can approach such a HIPed cermet being loaded into a larger HIP can filled with a filler metal where the latter case could actually even include three separate metal phases, i.e., metal used in cermet, metal in annular region, and metal HIP container material(s).[63] This design strategy provides depth-of-defense where breach of the cermet surface would not leach radioisotopes into the environment.

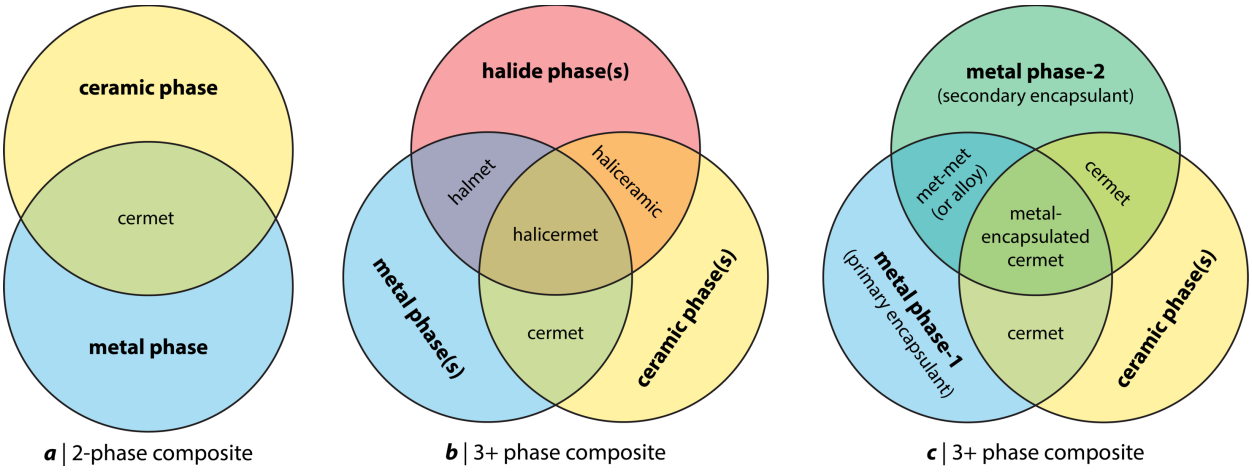

Figure 2. Venn diagrams showing the relationships between different potential phases present in a multi-phase waste form with accepted names for some and proposed names for others including (a) common ceramic-metal (cermet) composite, (b) the same as (a) but with halides phases present, and (c) a cermet with two metal phases. The "met-met" region in (c) could represent a 2-phase metal mixture, an alloy, an intermetallic, etc.

The design of a cermet waste form can include a variety of approaches, such as a two-phase composite (one metal and one ceramic waste phase) or a three-phase composite (i.e., one continuous metal phase, a ceramic waste phase, and an enveloping metal phase). Additional formulations could be envisioned from this starting point where more than one ceramic waste phase was included in the composite or mixtures of metals were used. In Figure 3, some general concepts are shown at a rudimentary level for visualization purposes. Figure 3a-c show ideas where both have a contiguous metal encapsulant phase surrounding the ceramic waste phase; however, this is shown with differing levels of volumetric waste loading (i.e., different waste packing densities). The concepts shown in Figure 3d-f show similar packing densities but with a secondary encapsulant metal containment phase. This could include a mixture of metal particles added prior to pressing or also represent metal canisters of different thicknesses such as a HIP canister. The effects of volumetric waste loading (V_{wl}) are shown below each panel in Figure 3, with the goal being to create a cermet waste form with minimal open porosity. Having too many phases present that have different compressibilities, malleabilities, and ductilities can lead to unforeseen issues during the consolidation process leading to residual porosities in the final form.

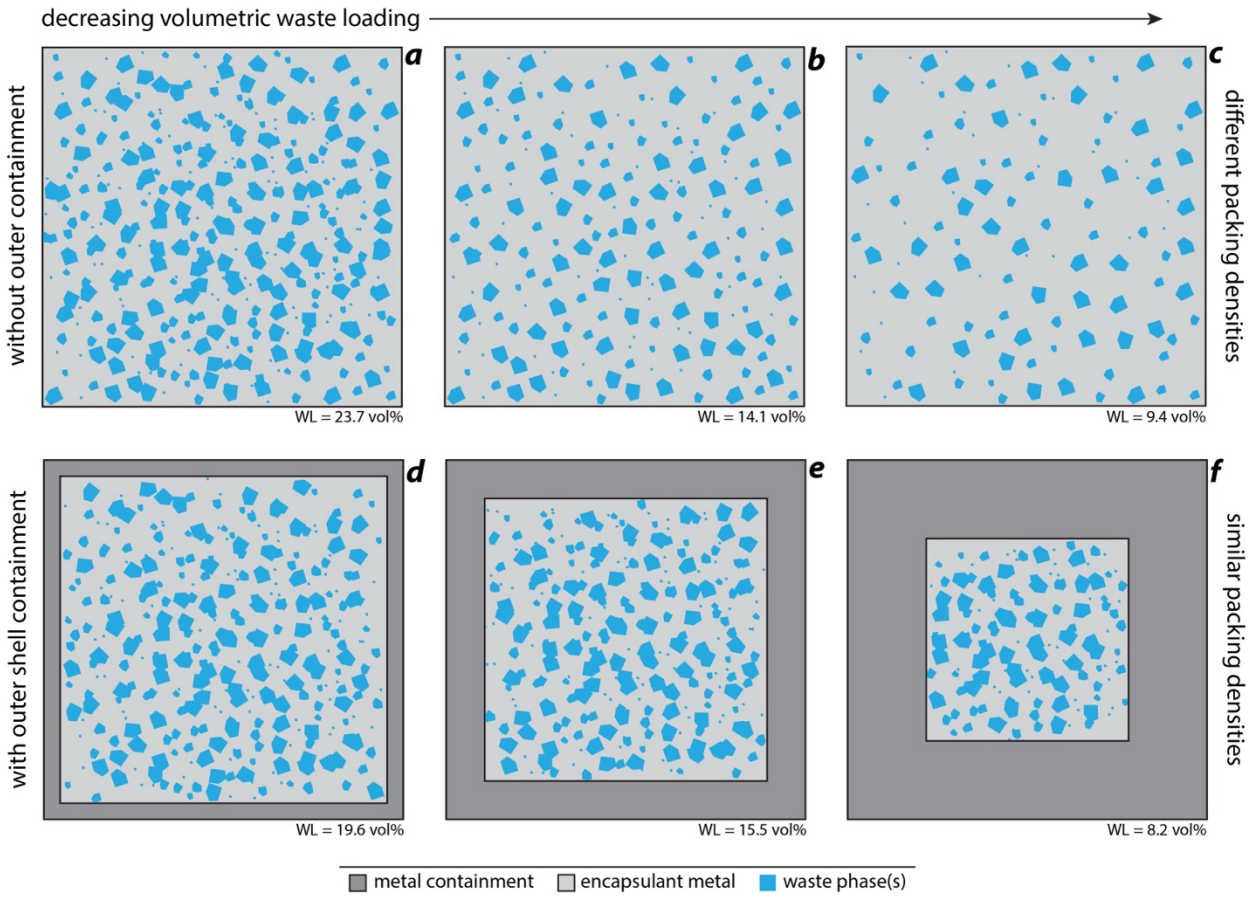

Figure 3. Design concepts for cermet waste forms including (a-c) 2-phase or (d-f) 3-phase processes. In each set (top, bottom) the volumetric waste loading is shown to decrease from left to right. Volumetric fractions of the waste phase(s) (blue phase) are shown in the bottom right corner below each example.

In terms of the mixtures of materials going into the composite waste form, several options exist that could include (1) premixing the phases and pressing directly, (2) size reducing the materials separately or together prior to fabrication (e.g., through ball milling), or (3) using a core-shell process whereby an inner containment is encapsulated by an outer containment (e.g., HIP can in a HIP can – see Figure 4). Creating mixtures with differently sized fractions can result in more heterogeneous distributions of the target phase within the encapsulant.

Selecting the ideal ratio of waste to encapsulant is important, which must be done on a volumetric and mass basis, which is based on the densities of the different phases present where the waste form volume (V_{wf}) can be calculated as a sum-product of the specific volumes (v_i) and masses (m_i) of each phase (i) present in the composite, see Equation (1). The total mass of the waste form (m_{wf}) is equal to the sum of the

individual component masses (m_i) as shown in Equation (2). In an ideal multi-phase waste form, the encapsulant phase should be contiguous (interconnected) and fully encapsulating the material of interest to limit release of the waste from the composite waste form, in the event that the encapsulant layer were breached within a repository. The volumetric waste loading (V_{wl}), or the volume of waste in the final composite waste form, is calculated using Equation (3) where v_w is the specific volume of the waste phase(s) and m_w is the mass of the waste phase(s). Equation (4) can be used to determine the waste loading on a mass basis (m_{wl}) using previously defined variables.

$$V_{wf} = \sum_{i=1}^{n} v_i m_i \tag{1}$$

$$m_{\mathrm{wf}} = \sum_{i=1}^{n} m_i \tag{2}$$

$$V_{wl} = \frac{100 \cdot (v_w m_w)}{\sum_{i=1}^{n} v_i \, m_i} \tag{3}$$

$$m_{wl} = \frac{100 \cdot (m_w)}{\sum_{i=1}^{n} m_i} \tag{4}$$

Specific volume (v_w) is calculated using Equation (5), where V_i is the volume of the ith component and m_i is the mass of the ith component. The fraction of theoretical specific volume ($v_{theor.}$), i.e., inverse density, can be calculated using Equation (6), where v_m is the measured specific volume. In the former case, Equation (5), the specific volume is useful to compare cermets with varying compositions and processing methods. In the latter case, Equation (6), the percentage of theoretical specific volume can be used to compare cermets prepared with the same composition but different processing methods. Equation (5) and Equation (6) assume no side reactions between phases.

$$v_w = \sum_{i=1}^{n} \frac{V_i}{m_i} \tag{5}$$

$$v_{theor} = \frac{v_m}{\sum_{i=1}^{n} \frac{V_i}{m_i}} \quad (6)$$

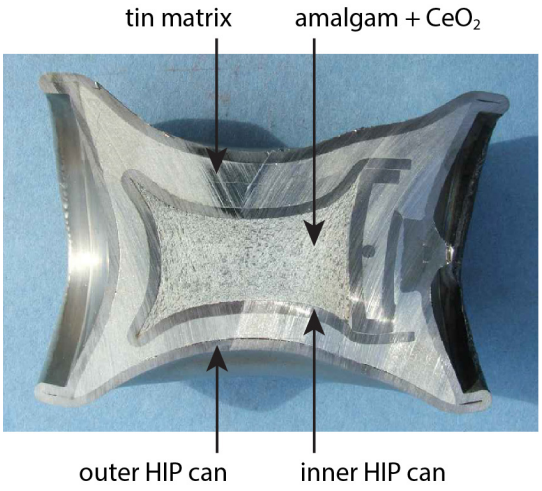

Figure 4. Cermet made with an Hg-Sn amalgam + CeO_2 in the core inside an inner HIP canister and Sn metal in the annulus region between the inner HIP canister and outer HIP canister.[63] This image was modified from the original by Maddrell[63] and reprinted with permission. Copyright Nuclear Decommissioning Authority 2011.

When designing radioactive waste forms, waste loading characteristics are critical to understanding the final waste volume and thus repository size, where higher waste loading reduces the final waste form. In cermet design, it is common to find ceramic-phase loading as high as 80 mass%.[2,64] Figiel et al.[65] found that the hardness and Young's modulus of a 90 vol.% TiC–(Ni, Mo) cermet exceed that of the 70 and 80 vol%-TiC cermet. Dias et al.[66] studied WC-Cu cermets with 50 and 75 vol.% WC prepared via hot-press, as thermal barriers in the first wall of nuclear fusion reactors. It was found that the 75 vol.% WC had superior hardness and elastic modulus. Based on these results, it is plausible that to design a cermet waste form with high radioisotope loading.[2,64]

3.1 Wettability

An important parameter to consider in cermet design is the wettability between the ceramic and metallic phase within the cermet. Many composite systems comprised of a metallic binder phase and a ceramic reinforcement phase have been developed where high-strength and lightweight are desirable properties.[2,67-69] In ex-situ processing methods, reinforcement phases, such as carbides or nitrides are added

to a molten-metal and cast to the desired geometry. However, poor wettability can cause particle agglomerations, poor interfacial bonding, and reduced mechanical strength. As such, many studies have undertaken investigations to improve the wettability between various ceramic and metallic phases.[51,69-72]

Malaki et al.[73] defines wettability not only by the contact angle, discussed below, but also the dispersion, engulfment, and distribution of reinforcing particles. There are many factors that have a strong influence on wettability, such as contaminates, particulate size, intermetallic formation, chemical composition, surface chemistry and roughness, density, temperature, crystallographic orientation, and time of contact.[73] For a detailed examination on the general effects of each parameter the reader is directed to reference.[73] Given the considerable number of metallic-ceramic phase combinations that can exist in a nuclear waste form, as previously mentioned, significant effort should be undertaken to improve the wettability of the composite to the greatest extent practical.

Wettability is determined by interfacial energies contained within the material system. This relation can be seen in Equation (7), where θ is the wetting angle, and γ_{sv}, γ_{sl}, and γ_{lv}, are interfacial energies of the solid-vapor, solid-liquid, and liquid-vapor, respectively.[73] In general, good wettability refers to a low-contact angle, where the liquid spreads out over the solid grain. To reduce the contact angle (θ), the solid-liquid or liquid-vapor interfacial energies are reduced, or the solid-vapor interfacial energy is increased. Equation (7) can be expanded to Equation (8) to include the volumetric dependence and the effect of the Laplace pressure, where α is the droplet radius, and *k* is the line tension.

$$\cos(\theta) = \frac{\gamma_{sv} - \gamma_{sl}}{\gamma_{lv}} \tag{7}$$

$$\cos(\theta) = \frac{\gamma_{sv} - \gamma_{sl}}{\gamma_{lv}} + \frac{k}{\gamma_{lv}}\frac{1}{\alpha} - \frac{\gamma}{\gamma_{lv}}[2 + \cos(\theta) - 2\cos^2(\theta) - \cos^3(\theta)] \tag{8}$$

One of the most widely studied systems are the WC-metal and Ti(C,N)-metal cermets for use as cutting tools. WC has been reported in many applications due to its combination of favorable properties, such as hardness and wettability by molten metals.[74] However, use as structural components in elevated temperatures has been avoided due to their poor oxidation resistance and high density.[70] In the WC-Co

system the cobalt completely wets the WC phase ($\theta = 0°$).[75] In contrast, a contact angle greater than 90° results in effusion of the liquid metal to the cermet surface, deteriorating mechanical properties. To empirically determine the wettability of a system, the sessile drop method is commonly employed, where the contact angle is measured. This measurement is typically made from (400 to 2000) °C.[73]

A large body of research has also been conducted on MMCs with nano-reinforcement phases. However, nano-reinforced MMCs produced via liquid processing techniques suffer from poor homogeneity due to the high interfacial energy between the molten metal and the reinforcement particle phase resulting in poor wettability.[76] As such, the nanoparticles are susceptible to agglomeration, generating a heterogenous dispersion throughout the matrix, due to the high viscosity and surface tension in the molten-metal melt.[68] Zheng et al.[71] studied nano-Ti(C,N) powders in a Ni-Mo matrix and found that oxygen contamination during sintering of nano-Ti(C,N) powders resulted in a decrease of the solid-vapor interfacial energy (γ_{sv}), increasing the contact angle between the ceramic and metallic phase. As the contact angle increases, wetting decreases, reducing the density of the cermet and deteriorating mechanical properties. To improve wettability, several investigations have studied novel processing methods, such as high-intensity ultrasonic waves to incorporate nanoparticles in the MMC.[77,78]

Considering nuclear waste forms, cermets may complement other waste forms such as vitrified wastes, which suffer from nepheline formation due to high sodium and aluminum content, and low thermal conductivity.[18] It may be possible to design a cermet which takes advantage of spent fuel reprocessing waste which has a high-aluminum and/or magnesium content from certain fuel cladding designs. For example, waste high in magnesium and aluminum such as Magnox sludge waste may inherently have good wettability characteristics. In MMCs, magnesium scavenges oxygen from the matrix-particle interface, thereby reducing the contact angle and improving wettability.[79] In an aluminum matrix magnesium forms high-wettability phases such as $MgAl_2O_4$ through Reaction (9) and Reaction (10) shown below.

$$3\ Mg + Al_2O_3 \rightarrow 3\ MgO + 2\ Al \quad (9)$$

$$3\ Mg + 4\ Al_2O_3 \rightarrow 3\ MgAl_2O_4 + 2\ Al \quad (10)$$

Similarly, Zr, which remains metallic following processing of SNF, decreases the surface tension and lowers the reinforcement-matrix interfacial energy, improving wettability.[73] Post-mechanical treatments, such as stir casting or ultrasonication, can improve wettability as well.[73] However, for nuclear waste form design, post-mechanical treatments should consider other risks, such as radioisotope volatilization.

3.2 Powder Metallurgy

Powder metallurgy is any fabrication process which uses metallic powder as the precursor binder material mixed with a hard-ceramic dispersed phase for reinforcement. Several reviews exist discussing powder metallurgy routes to fabricate MMCs.[47,48,67,80] Chaira et al.[48] provides a detailed analysis of the state-of-the-art for powder metallurgy. Manohar et al.[76] discusses applications of powder metallurgy, specifically mechanical milling methods, to eliminate defects from MMCs prepared via stir casting, squeeze casting, and other conventional techniques.

In powder metallurgy, the precursor powder material can be produced via machining, milling, mechanical alloying, electrolytic fabrication, chemical reduction, and atomization.[48] The precursor powder is then mixed with lubricants and additives, such as polyglycol or paraffin wax, milled to homogenize the powder and fragment agglomerates, and compacted prior to final processing. Conventional powder compaction is performed using a die and punch assembly (see Figure 5), however the die process can produce density gradients within the final compact. In single action pressing, pressure as a function of distance from the die face can be calculated using Equation (11) Where P_x is the transmitted pressure at position x, P is the pressure applied at the top of the punch, D is the diameter of the compact, and z is the proportionality constant (radial stress/axial stress).[48] To reduce density gradients within the green compact, cold isostatic pressing (CIP) can be used to produce a more uniform pressure within the compact.

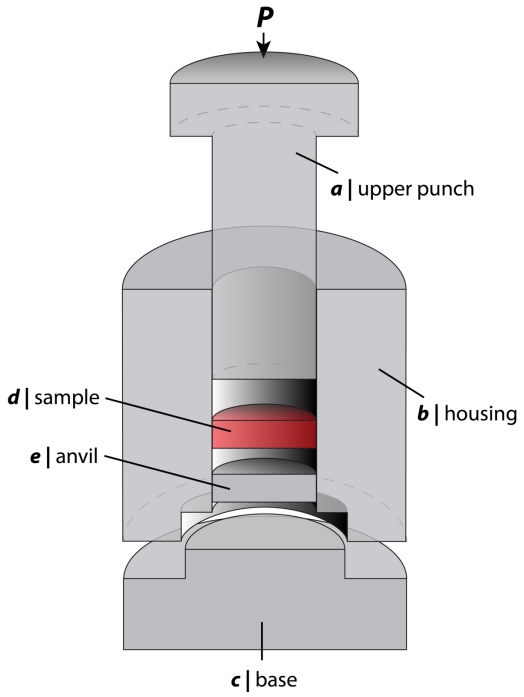

Figure 5. Typical die and punch assembly used to press powder into a green compact prior to final processing showing (a) the upper punch, (b) the housing, (c) the base, (d) the sample, and (e) the anvil. In this setup, the pressure (*P*) is applied from the top on the upper punch.

$$P_x = P \cdot \exp\left(-\frac{4uzx}{D}\right) \tag{11}$$

Al-Qureshi et al.[81] developed a model to predict the final density of the green compact powder based on an axisymmetric solution of large deformation. This is shown in Equation (**12**) where P_t is the theoretical density of the material, P_p is the tap density, P_a is the applied external pressure of the punch, $\overline{\sigma}$ is the effective stress in compression of the bulk material, μ is the container-compacted powder interface, H is the distance of the element from the top surface compact-instantaneous, Z is the current height of the element, and r is the current radius of the element.

$$\rho_g = \rho_p + \left(\rho_t - \rho_p\right)\left[1 - exp\left\{-\left(1 - \frac{P_a}{\bar{\sigma}}\right)e^{\mu(H-2Z)/r} + 1\right\}\right] \tag{12}$$

Their results agree well with published experimental values. A full derivation was provided by Al-Qureshi.[81] Following compaction, final processing includes techniques such as, sintering, hot uniaxial

pressing (HUP), HIPing, spark plasma sintering (SPS), microwave sintering, powder forging, powder rolling, powder extrusion, and dynamic powder compaction. Advantages of powder metallurgy routes over other methods are lower energy consumption, higher material utilization and reduced number of processing steps.[48]

3.3 Pressureless Sintering

Pressureless sintering is a fabrication method where the powder components are homogenously mixed, typically in powder form, pressed into a green compact and heated without pressure, to form the final product. In terms of a nuclear waste form, advantages of this process are, simplicity and cost effectiveness, and reduced risk of impurity contamination.

During sintering, temperatures 0.7 – 0.8 of the melting temperature are applied to bond particles. Here the driving force is the reduction in surface energy. In cermets, the microstructure develops with the formation of a core and rim structure, see Figure 6.[82] It is known that the core and rim structure strongly influence the final mechanical properties of the material; however, no studies have investigated the effect on chemical durability, which would be informative to the nuclear waste form community. Pörnbacher et al.[82] found that the rim phase in TiC-steel composites has a NaCl crystal structure and grows epitaxially on the TiC particle surface.

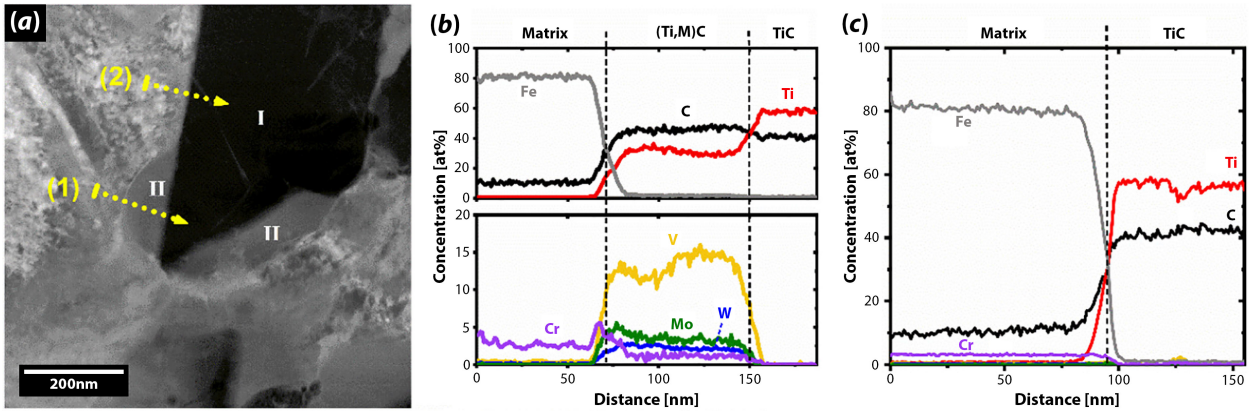

Figure 6. (a) Scanning transmission electron micrograph of a mechanically blended sample including energy dispersive X-ray spectroscopy (EDS) line scan positions 1 and 2. TiC and rim phases are marked with I and II, respectively. (b) Results of the EDS line scan on position 1 including matrix, (Ti,M)C and TiC (c) and position 2 including matrix and TiC. This figure was reprinted with permission from Pörnbacher et al.[82] Copyright Elsevier 2019.

3.4 Liquid Phase Sintering

Liquid Phase Sintering (LPS) is a technique similar to pressure-less sintering; however, components are added which aid in the densification of the final product improving the efficiency of the process. In LPS, typical precursor material consists of 5-15 vol.% liquid. While this method is normally considered to improve densification of ceramic materials, the potential enhancement in waste loading achievable for cermets makes LPS highly relevant. In this method, constituents within a multi-component powder consist of high-melting point ceramic phases and a low-melting point wetting phase.[51] During the sintering process, the ceramic phase is present alongside the wetting liquid. For non-interacting systems, good wetting results in grain rearrangement and densification from capillary forces exerted by the wetting liquid.[51] For interacting systems, a high solid-solubility in the liquid and a low liquid-solubility in the solid is ideal.[51] Figure 7 shows expected results based on solubilities during initial compact heating.[83-86] Since diffusion occurs within the liquid, LPS requires low-temperatures and reduced times compared to conventional sintering.

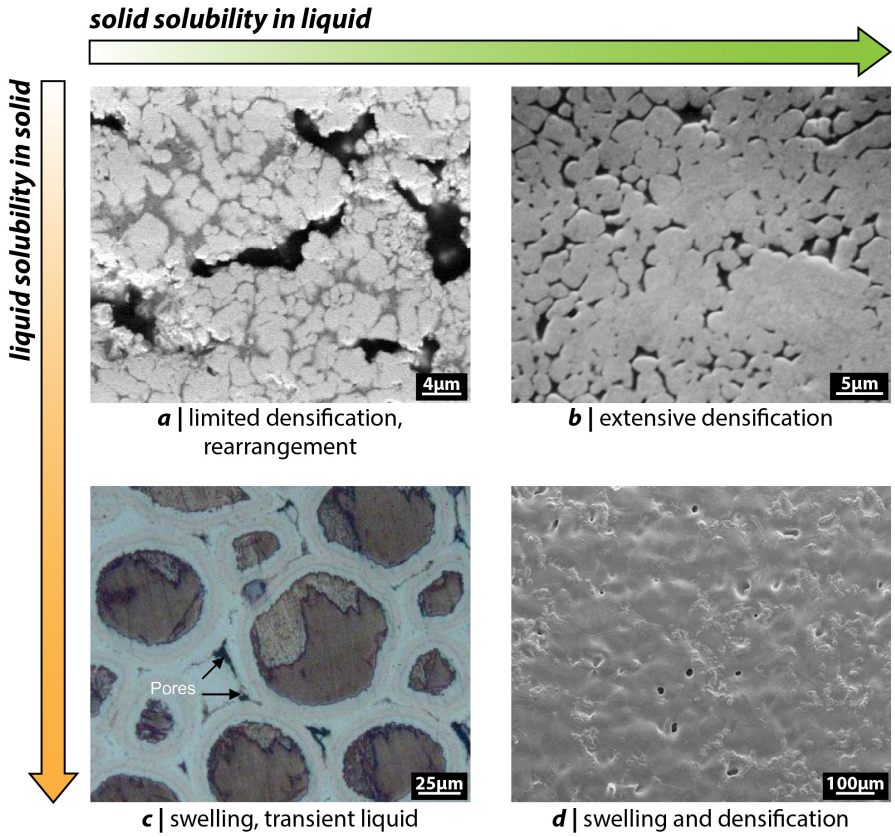

Figure 7. Behavior expected during initial compact heating base on relative solubilities of the two phases including (a) W-20Cu produced from initial W particle size of 1.08 µm,[83] (b) W-9Cu-1Ni sintered at 1500°C for 1 h,[84] (c) Al-Ti showing Al around Ti particles,[85] and (d) Ti-5Si compacted at 600 MPa and sintered at 1350°C for 2 h.[86] Images were modified from the originals with permission and this collage is based off a concept provided by German et al.[51] Copyright Springer 2008.

One of the important characteristics of the final material is grain size, where the cumulative grain size distribution can be predicted in three-dimension by Equation (13), where G is the true grain size, c is the scale parameter related to the median grain size, and m is the shape parameter.[51] Another key waste form characteristic is the final density of the material. If a good final density can be achieved at lower temperatures the process is more cost effective. During LPS a large reduction in the melt formation temperature lowers the overall sintering temperature, see Figure 8.

$$\mathrm{F}(G) = 1 - \exp\left[-\left(\frac{G}{c}\right)^{m}\right] \tag{13}$$

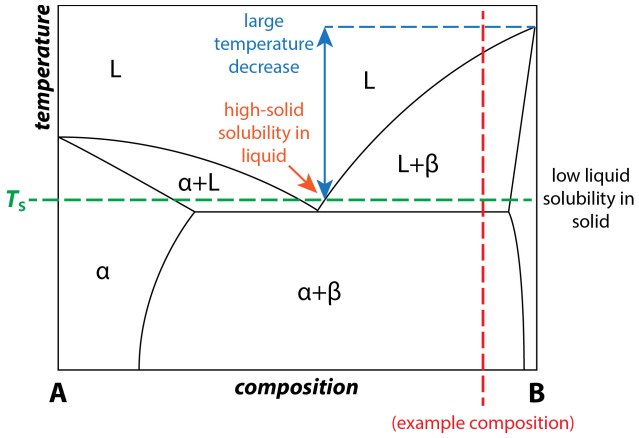

Figure 8. An example phase diagram showing a reduction in melt formation temperature. The sintering temperature (T_S) here reduces overall cost of the system while providing good solid solubility in the liquid. In this binary phase diagram, phases α and β are represented along with the liquid (L) phase. This figure was reprinted with permission from the original publication by German et al.[51] Copyright Springer 2008.

3.5 In-Situ Processing

In-situ processing of MMCs may be one of the more beneficial methods for disposition of advanced reactor waste streams containing salts. In this method, a reaction between the salt and the matrix results in formation of secondary phase particles.[47] The secondary phase reinforcement particles can be considered stable within the composite due to the energetically favorable reaction. Davies et al.[87] produced the first Al-TiB_2 MMC using in-situ processing. Salts K_2TiF_6 and KBF_4 were added to a molten aluminum matrix resulting in the formation of an Al-TiB_2 composite. Fluoride-based salts from MSRs requiring disposition, such as LiF_2-BeF_2 (FLiBe) and LiF-NaF-KF (FLiNaK) may be good candidates for in-situ processing methods to stabilize secondary phases followed by encapsulation in a secondary HIP containment. Advantages over other processing methods include reduced contact angle, resulting in improved wetting and improved bonding strength. However, it has been reported that the secondary phase particles prefer to segregate along the grain boundaries.[88] It would be useful to evaluate if secondary phase particle segregation along grain boundaries degrades chemical durability; however, no studies, to the knowledge of the authors, have been undertaken. Regardless, investigations attempting to produce cermets from salt-waste streams via in-situ processing would benefit the radioactive waste disposition community.

3.6 Ultrafast High-Temperature Sintering

One of the more novel methods in recent literature imposed to combat several problems that arise during cermet sintering, such as metal volatilization, radioisotope volatilization for radioactive waste forms, grain coarsening, and poor wettability, is the ultrafast high-temperature sintering (UHS) method. Here, Guo et al.[50] studied the effects of sintering a 20 vol.% Ni-based superalloy and 80 vol.% Al_2O_3 using UHS, which led to improved wettability, grain growth control and reduced volatilization due to short sintering times. Density for traditionally sintered pellets and UHS pellets were 3.78 g cm^{-1} and 4.67 g cm^{-1}, respectively. Figure 9 depicts optimal sintering temperatures and times to maximize composite density for this technique.

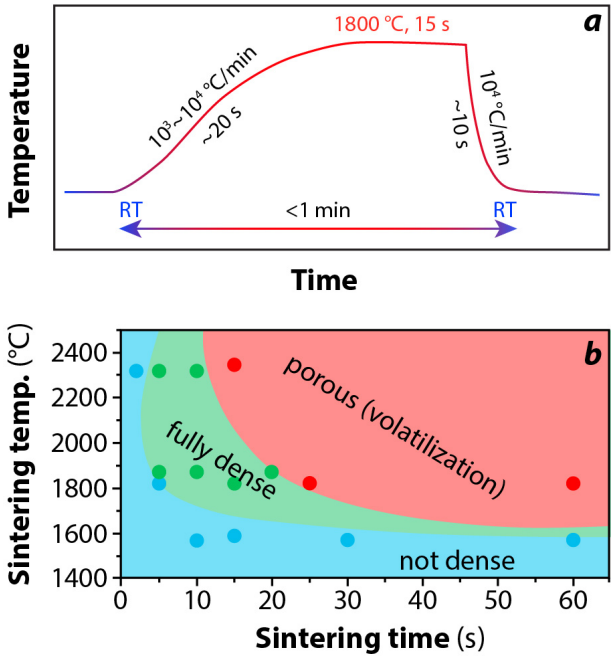

Figure 9. (a) Time-temperature (furnace) diagram for UHS. (b) time-temperature transformation diagram showing optimal cermet transformation conditions. This figure was reprinted with permission from the original work by Guo et al.[50] Copyright Elsevier 2021.

3.7 Mechanical Milling

The primary technique for mechanical alloying and particle size reduction is ball milling, where particles are placed in a vial with media and energy is imparted into the system via high energy collisions. These collisions result in repeated fracturing and rewelding of the material, which generates very fine

particles, on the order of micrometers to nanometers. Manohar et al.[76] lists several MMCs which have been successfully fabricated via mechanical milling, such as 316L + polycarbosilane (PCS), several aluminum alloys, and copper + Graphene-nano-sheets.

3.8 Hot-Pressing Techniques

There are two common hot-pressing methods used to produce cermets or MMCs, HUP and HIP. The HUP method is similar to powder compaction prior to sintering, except heat is applied simultaneously with pressure. The powder may be pressed directly within the die, or the powder may be sealed in an evacuated bellows-type container, which allows compaction while preventing cross contamination with the die and punch, as well as preventing the material from volatilizing. Because the material is compacted and sintered using a die and punch assembly, pressure gradients and thus density gradients can form in the material, generating undesirable material properties.[48]

HIP resolves problematic density gradients produced in the HUP process by applying isostatic pressure, compressing the compact in all directions simultaneously.[48,89] In this method, the powder is packed into a thin-walled metal container, heated and compressed under an inert gas. Prior to compression, the canister is evacuated of atmosphere, so that during the hot-pressing process, the void spaces between the particles in the canister can be readily filled during compaction. During HIPing, the defects within the preform collapse and diffusion bonding takes place.[89] Considering radioactive waste forms, advantages of HIPing in a canister are achieving theoretical density of the material with limited grain growth and encapsulation in an impermeable membrane. It has been shown that a bimodal or continuous particle size distributions results in improved densification over “monosized” powders.[89]

Although originally developed for diffusion bonding nuclear fuel and cladding, it has also been used for processing nuclear waste forms. The Australian Nuclear Science and Technology Organization (ANSTO) developed a HIP method to press problematic nuclear wastes into dense monoliths.[90] In this method, simulated plutonium wastes, HLW from Idaho calcines and Magnox sludges were pressed into a monolithic waste form using a HIP process.[8] A 85 mass% zeolite (clinoptilolite + mordenite), 10 mass% sand, and 5 mass% Magnox sludge mixture was HIPed to a dense waste form with 98 mass% waste loading.

ANSTO has also successfully HIPed a 0.4 kg sample containing ~50 g Pu for disposal of surplus impure weapons grade Pu. This was scaled to 10 kg using Ce as a Pu simulant. While studies have successfully immobilized radioisotopes, such as Pu in a dense cermet waste form, further studies should be undertaken to investigate long term waste form integrity. For example, alpha-decay and helium deposition within the waste form can lead to an increase in internal pressure and material degradation.

3.9 Spark Plasma Sintering

Spark Plasma Sintering (SPS) uses electric current to consolidate and reaction-sinter materials. Other nomenclature found in literature for this method are pulsed electric current sinters, field-activated sintering technique (FAST), and current-activated pressure-assisted densification.[91] Advantages of this method include lower sintering temperature and shorter sintering times while reaching near theoretical density and reduced grain growth compared to traditional pressureless sintering.[91-93] In this method, the applied electric field has a strong effect on the final composite material. For example, in Figure 10, three Al-Au layered composites were fabricated at 500 °C for 4 h with increasing current densities. It is clearly shown that intermetallic growth is strongly influenced by the current density. Chen et al.[94] revealed that SPS produced materials have lower impurity levels in the grain boundaries.

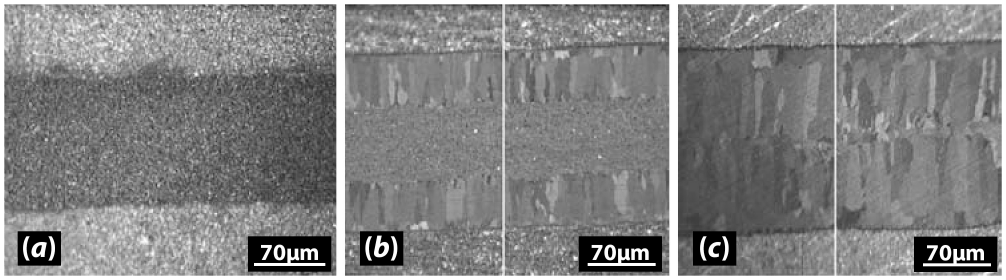

Figure 10. Effect of electric current on intermetallic growth in a layered Al-Au composite preform. Intermetallic growth increases as current density increases. (a) no current, (b) $J = 0.51\times10^3$ A cm^{-2}, and (c) $J = 1.02\times10^3$ A cm^{-2}. This graphic was modified with permission from the original by Bertolino et al.[95] Copyright Elsevier 2001.

Nečina and Pabst[96] investigated the effects of alkali halide additives on spinel ceramics, including LiF, LiCl, NaCl, KF, and KCl, produced via SPS. They found that spinel produced with LiF and NaF improve densification; however, NaF also inhibits grain growth, while LiF promotes grain growth. They

attribute the accelerated grain growth to the Li^+ ion. These alkali halides are frequently added as sintering aids for polycrystalline ceramics.

4 Cermet Properties

4.1 Thermal Conductivity

Enhancements in overall waste form thermal conductivity could offer advantages for immobilization of radioisotopes that generate significant amounts of radiogenic heat by lowering centerline temperatures to minimize material degradation (i.e., centerline is the temperature at the center of a cylindrical specimen). These concepts pertain to decay heat tolerance for that waste form, which is defined as the limits on the chemistry, structure, and mechanical properties imposed by the amount of heat generated by the decay of high-activity radionuclides. Two of the primary high-heat dose contributors are ^{137}Cs ($t_{1/2}$ = 30.17 y) and ^{90}Sr ($t_{1/2}$ = 29.1 y) that decay through β^- emission.

For waste forms that contain high-heat producing radioisotopes, it is crucial to understand the thermal history to ensure long-term waste form stability. In particular, excessive centerline temperatures are a concern in various waste packages. For example, a vitrified waste form might have waste loading limitations to avoid high centerline temperatures caused by the temperature gradient (center to edge) that occurs from its configuration and intrinsically low thermal conductivity. If these structural changes occur above the glass transition temperature (T_g), this can lead to unwanted crystallization of certain phase (e.g., nepheline) and reduced chemical durability of the waste form.[97,9845] These centerline temperatures can be improved by utilizing a waste form that exhibits suitable heat transferability. It is important to note that other properties and environmental conditions, such as specifications of the waste package, surrounding geology, radioisotope inventory, and repository loading, play a critical role in understanding the centerline temperature.

This decay heat tolerance can be much higher in a metal-containing waste form due to both the high thermal conductivity and high melting temperatures for most of the key encapsulant metals of interest, even when combined with ceramic phases that exhibit low thermal conductivities. Finally, metal-containing waste forms offer significantly higher densities of commonly employed metals (ρ_b > 6 g cm^{-3}). The higher

ρ_b values of the metal phase used, the lower the overall volumetric storage for the composite waste form than if this phase was replaced by something of lower ρ_b such as a glass or ceramic phase; these generalizations assume no open porosity introduced by changing the encapsulant phase. For these reasons, in cermet waste form design, thermal conductivity emerges as a critical material property, which, if tailored appropriately, provides the customer with increased flexibility in selecting a suitable repository. This is especially important for short-cooled fuels coming out of a reactor and less of an issue after a few $t_{1/2}$ of the high-heat producing radioisotopes present.

4.1.1 *Measurement Methods*

Numerous methods of experimentally determining thermal conductivity exist, with one of the most well established and common methods for measuring thermal conductivity and thermal diffusivity being Laser Flash Analysis (LFA), developed by Parker[99] in 1961. This absolute method which is summarized under ASTM E1461,[100] involves irradiating the specimen surface with a laser or another heat source, then taking a temperature-time measurement from the reverse side of the material. This temperature curve can then be used in conjunction with the thickness of the sample to determine thermal diffusivity (α). Furthermore, thermal conductivity (k) can then be calculated using the Equation (14) where units of k are W m^{-1} K^{-1}, α has units of m^2 s^{-1}, ρ is density with units of kg m^{-3} (which can be measured with a dilatometer as a function of temperature), and c_p is specific heat capacity with units of J kg^{-1} K^{-1} (which can be measured with a differential scanning calorimeter or a drop calorimeter as a function of temperature).

$$k = \alpha \cdot \rho \cdot c_p \tag{14}$$

This transient technique eliminates the factor of thermal contact resistance and has the advantage of being able to test small specimens at a rapid rate at various temperature ranges.[99,101] This technique, however, is subject to a possible 10% error, and is most ideal for specimens that are solid, homogenous, and isotropic, as stated by Parker[99] and as detailed in ASTM E1461 sections 1.7 and 1.7.1.[100]

A promising modern technique that can be used to determine thermal conductivity is the transient hot bridge (THB) method. This procedure involves a sensor and heating element being sandwiched between

two identical samples, and has the benefit of being able to analyze materials at a rapid rate and at various temperatures.[102] This method is interfacial in nature and creates an inhomogeneous temperature profile by applying heat in a non-uniform distribution.[102] An interesting potential of this method is the ability to measure direction dependent thermal conductivity values of anisotropic materials. This allowed Lagüela et al.[103] to determine the direction dependent thermal conductivity of oak wood in three dimensions. Gaiser et al.[104] proposed a procedure that combines THB with finite element analysis to determine thermal diffusivity values in the three special directions by means of orientation of the sensors, and found that the measurement uncertainty was 4% to 10%. This method is still fairly new, and thus does not yet have the same set of standards (such as a technique specific ASTM) as other more established methods.

4.1.2 *Models*

Due to the heterogenous, anisotropic nature of cermets, it may be beneficial to use mathematical models and other interpretations to supplement existing experimental methods. Various mathematical models and estimations have been proposed and developed over the years to estimate the thermal conductivity of heterogenous materials. The effective thermal conductivity of binary phase material with a discontinuous phase dispersed in a continuous matrix can be modeled as a series of parallel or perpendicular laminae, or as layers in a cubic lattice, and then solved by utilizing the addition of series and parallel resistances using Ohm's law.[105,106] However, these models assume one dimensional heat flux, in which the flow lines are assumed to travel in a straight line.[105,106] In reality, the flux lines will bend towards or away from the discontinuous phase,[105,107] and thus the Ohm's law models may not provide adequate accuracy in materials that contain high conductivity ratios between phases, which Powers describes as ratios past 10:1.[105] This review will instead focus on models based on flux laws, as cermet materials most often exhibit high conductivity differences between the ceramic and metallic phases, and thus the effects of field interactions will have to be considered (see Figure 11).

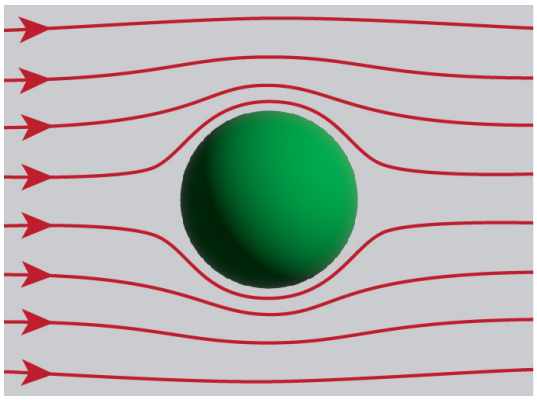

Figure 11. Illustration of the particle field interactions around a spherical particle that is suspended in a much more conductive matrix material, $k_m >> k_p$. Note that the flux lines will return to a more linear state as distance from the particle increases. This figure was redrawn with permission from the original by De La Rue and Tobias.[107] Copyright The Electrochemical Society, Inc. 1959.

Early interpretations based off flux laws were developed by Maxwell[108] and Rayleigh.[109] Maxwell analyzed a scenario in which the discontinuous particles in a continuous matrix were spherical and where interactions between the particles were assumed to be negligible.[108,110] Rayleigh[109] treated a similar case in which the particles were again spherical, but with interparticle interactions based off equally sized particles arranged into a cubic array.[110] Their relations would produce a model in which dilute concentrations of small, mono-sized particles with conductivities of k_p are suspended in a matrix material with a conductivity of k_m, represented in Figure 12d as the Rayleigh-Maxwell dilute dispersion Equation (15)[108,109,111] where, V_p is the volume fraction of the particle phase to the matrix phase, and k_{eff} is the overall effective conductivity of the composite material.

$$k_{eff} = k_m \left[\frac{2k_m + k_p - 2V_p(k_m - k_p)}{2k_m + k_p + V_p(k_m - k_p)} \right] \quad (15)$$

As the name implies, however, this equation is approximately limited to particle concentrations (discontinuous phase, V_p) of less than 10-15 volume percent (vol.%) due to the requirements for the particles to be spaced out in a way that the fields around each particle do not influence neighboring particles.[105,107,111] This would imply that this model may not be accurate for estimating the thermal conductivities of some cermet materials, as many cermets contain a ceramic phase that exceed those limits. Instead, another mathematical interpretation of the Rayleigh-Maxwell model, known as the Bruggeman

variable model [Equation (16) and Equation (17)],[112] should apply to dispersions of all concentrations of V_p,[105] and at various particle sizes.[105,113]

$$k_{eff} = k_p + (1 - V_p)(k_m - k_p)\left(\frac{k_{eff}}{k_m}\right)^{1/3} \quad (16)$$

$$(1 - V_p) = \left(\frac{k_p - k_{eff}}{k_p - k_m}\right)\left(\frac{k_m}{k_{eff}}\right)^{1/3} \quad (17)$$

Due to the dispersion type modeling, and the limits of integration performed, the Bruggeman variable equation is valid under the restrictive conditions that the dispersed spherical particles are completely surrounded by the matrix medium, and the continuous matrix phase is assumed to remain continuous from V_p = 0 to 100% (see Figure 12e).[105] It has been suggested that Equation (16) applies best when there is a large difference in dispersed particle sizes, as some studies demonstrate the relation becoming less consistent as the size difference of the dispersed particles decreased.[107,113] Meredith and Tobias[113] proposed a definition similar to the variable dispersion equation, in which the system was assumed to contain only two different particle sizes of equal volume fraction (Figure 12f), [Equation (18), simplification by Powers[105]], in contrast to the large range of sizes assumed by the Bruggeman variable dispersion model.

$$k_{eff} = k_m\left[\frac{4k_m + 2k_p - 2V_p(k_m - k_p)}{4k_m + 2k_p + V_p(k_m - k_p)}\right]\left[\frac{4k_m + 2k_p - V_p(4k_m - k_p)}{4k_m + 2k_p - V_p(k_m + 2k_p)}\right] \quad (18)$$

It is important to note that in both the variable dispersion model from Bruggeman (Figure 12e) and binary particle dispersion model from Meredith and Tobias (Figure 12f), it is assumed that the larger particle dominates the field interactions between particles, and thus field disturbance from the neighboring small particles are assumed negligible.[107,113] For conditions in which the spherical particles are no longer assumed to be completely surrounded by the matrix, another model from Bruggeman[112] [Equation (19)], which assumes a condition of spherical particles in a mixture can be used.

$$V_m\left(\frac{k_m - k_{eff}}{k_m + 2k_{eff}}\right) + V_p\left(\frac{k_p - k_{eff}}{k_p + 2k_{eff}}\right) = 0 \quad (19)$$

At low percentages of V_p, the Bruggeman mixture model,[112] shown in Equation (19), behaves similarly to conditions described by the dilute dispersion model shown in Equation (15) and described by Powers[105] (Figure 12a). However, as the volume of particles in the system increases ($V_p \approx 50\%$), the material no longer resembles a dispersion, and instead the particles are assumed to resemble a continuous phase (Figure 12b).[105] At extremely high values of V_p, the curve of the model resembles an inversion of the dilute dispersion theory, in which particles of the matrix material become dispersed in the now continuous particulate phase as $V_p \rightarrow 100\%$ (Figure 12c).[105] Miller,[111] in a study analyzing the practicality of these models for W-UO_2 cermet fuel applications, compared these three models (Rayleigh Maxwell "dilute", Bruggeman variable dispersion, and Bruggeman mixture)[108,109,111-113] as a function of V_p, and found that there was little variation between the three when V_p is low, with results deviating with the increase of V_p.

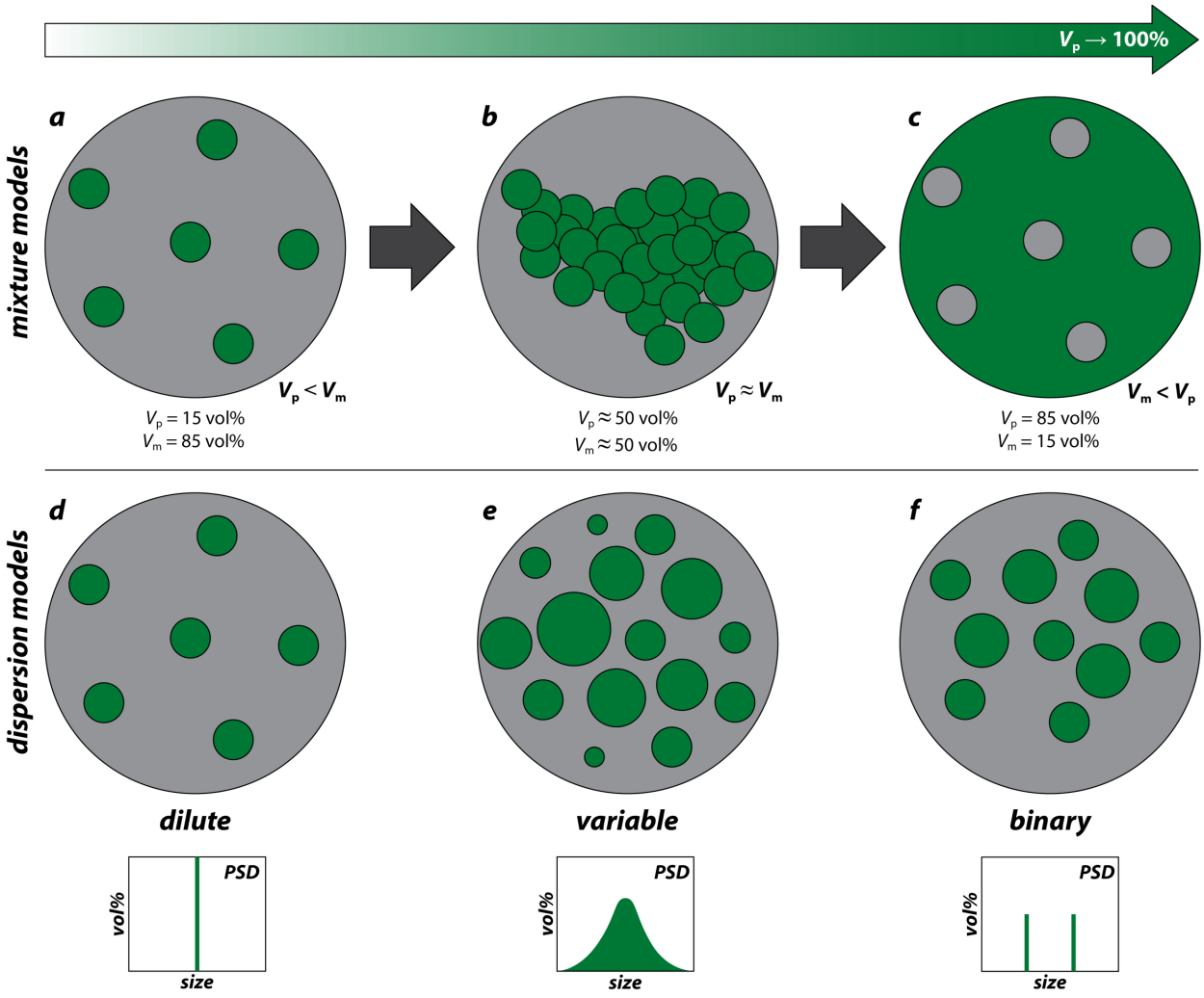

Figure 12. Representation of (a-c) mixture models [112] from Equation (19) and (d,e,f) dispersion models including (d) Equation (15) [108,109], (e) Equation (19) [112], and (f) a binary dispersion model by Meredith and Tobias [113]. Here, V_p = Volume fraction of the particle phase (vol%) (green), V_m = vol% of the matrix phase (gray), and PSD is the particle size distribution (%). Illustrations are not to scale.

Figure 13 compares of the spherical models discussed thus far as a function of k_{eff}/k_m to V_p (vol %). As noted by Powers,[105] the binary dispersion model from Meredith and Tobias[113] does not approach $k_{eff} = k_p$ as $V_p \rightarrow 1.0$. These aforementioned models, however, assume the particles to be completely spherical in nature, and might not accurately reflect some cermet materials after the manufacturing process.

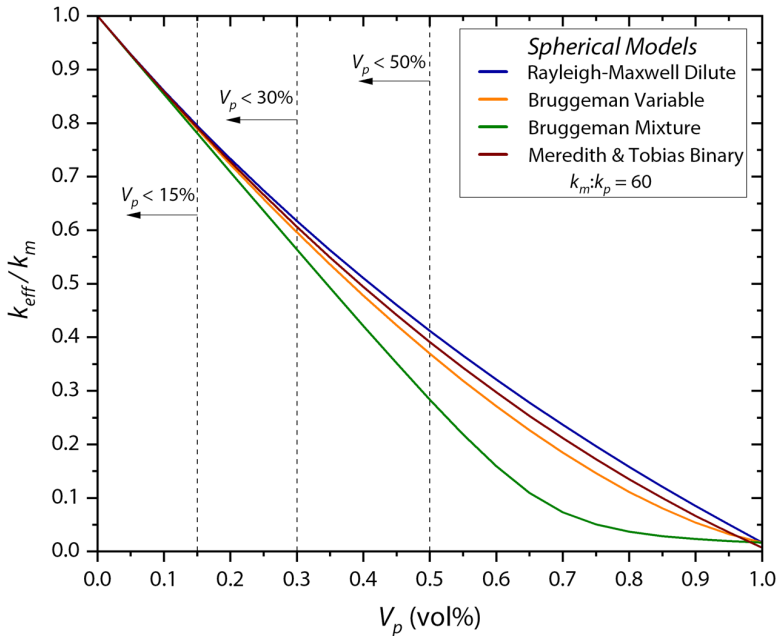

Figure 13. Comparison of spherical models in k_{eff}/k_m as a function of V_p for a material with a conductivity ratio k_m:k_p of 60. The models shown include those for Rayleigh-Maxwell Dilute model,[108,109,111] Bruggeman Variable model,[112] Bruggeman Mixture model,[112] and the Meredith and Tibias Binary Model.[113]

Anisotropic adjustments by the transformation *"X"* from Equation (20) can be applied to the Rayleigh-Maxwell Equation (21) and Bruggeman mixture Equation (22) with Fricke's work on randomly oriented ellipsoid shaped particles.[114] This modification can be useful for predicting thermophysical behavior in cermets, as some materials in literature have shown a change in geometry of the discontinuous phase following the pressing process.[111] Conditions in which two-directional preferred orientation of the particles take place can be seen in derivations shown in,[105] in which β represents a function of particle size and orientation (see Miller[111] for β values). Note that if the transformation *"X"* is equal to 2, Equation (21) and Equation (22) revert back to their original forms of Equation (15) and Equation (19), respectfully.

$$X = -\left(\frac{\left(\frac{k_p}{k_m} - 1\right) - \left(\frac{k_p}{k_m}\right)\beta}{\left(\frac{k_p}{k_m} - 1\right) - \beta}\right) \tag{20}$$

$$k_{eff} = k_m \left[\frac{Xk_m + k_p - XV_p(k_m - k_p)}{Xk_m + k_p + V_p(k_m - k_p)} \right] \quad (21)$$

$$V_m \left(\frac{k_m - k_{eff}}{k_m + Xk_{eff}} \right) + V_p \left(\frac{k_p - k_{eff}}{k_p + Xk_{eff}} \right) = 0 \quad (22)$$

The anisotropic correction can be applied to the mixture Equation (22) in the case where the concentration of particles and axial distortion is great enough to cause contact between particles. While not specifically defined, this would imply a potential lower bound of applicability of the anisotropic adjusted Bruggeman mixture model in the case where particle concentration and elongation are not high enough to cause significant interparticle interaction.[111] Powers[105] noted that these same anisotropic corrections are difficult to apply directly to the Bruggeman variable equation, due to the mathematical complexity of determining the value of the transformation "*X*" in Equation (19).[111] This leaves a theoretical gap in the mathematical models discussed thus far that can predict anisotropic conditions from $V_p \approx$ 15-50 vol.%, between the upper bound of dilute Equation (15) and hypothetical lower bound assumed by Miller[111] of the anisotropic mixture Equation (22). With the limitations of these equations in mind, Miller developed a model to predict the thermal conductivity of W-UO_2 cermet fuel for NASA's nuclear reactor applications.[111] Miller hypothesized that based on similarities between the Rayleigh-Maxwell dilute model and Bruggeman variable model in a material with spherical particles and a k_m:k_p ratio of 50, that "…*it appears conceivable, if not probable, that a relation would also exist if an anisotropic version of the variable dispersion model was available...*".[111] The model shown in Equation (23) is Miller's deductive interpretation of this hypothesis, which was proposed to be used in the scenarios where the composite design falls outside the regions of applicability of the individual equations.[111]

$$k_{Miller} = k_{Bruggeman:V} \left[\frac{k_{Fricke-Dilute}}{k_{Rayleigh:Maxwell}} \right] \quad (23)$$

Where k_{Miller} represents the hypothetical conductivity of a modified anisotropic Bruggeman variable equation, $k_{Bruggeman:V}$ represents the Bruggeman variable Equation (16) for spheres, $k_{Fricke-Dilute}$ represents k_{eff}

as determined by the anisotropic dilute dispersion Equation (21), and $k_{\text{Rayleigh:Maxwell}}$ represents k_{eff} as determined by the dilute dispersion Equation (15) for spheres. Johnson[115] opted for a different approach and determined a relation to apply the Fricke transformation Equation (20), directly to the Bruggeman variable model Equation (16). This would be known in literature as the Johnson model and is represented in Equation (24).

$$\left(1 - V_p\right) = \left(\frac{k_p - k_{eff}}{k_p - k_m}\right)\left(\frac{k_m}{k_{eff}}\right)^{1/(x+1)} \tag{24}$$

Note that Equation (24) will reduce back to the original equation when the transformation *"X"* is equal to 2. A comparison of these anisotropic models and their conventional applicable bounds can be seen in Figure 14, which portrays a material with a matrix to particle conductivity ratio of 60, and with a geometric transformation [see Equation (20)] of 4. In this example, it was found that the difference between the Miller[111] and Johnson[115] models were below 10% in the region Miller proposed his equation to be used ($15\% < V_p < 50\%$). Additional models for other complex cases that may pertain to cermets include the Maxwell-Eucken[116] and Levy[117] models for porous materials, or the Kerner[118] model for coated particles. Table 2 provides a summary of the analytical models discussed in this review.

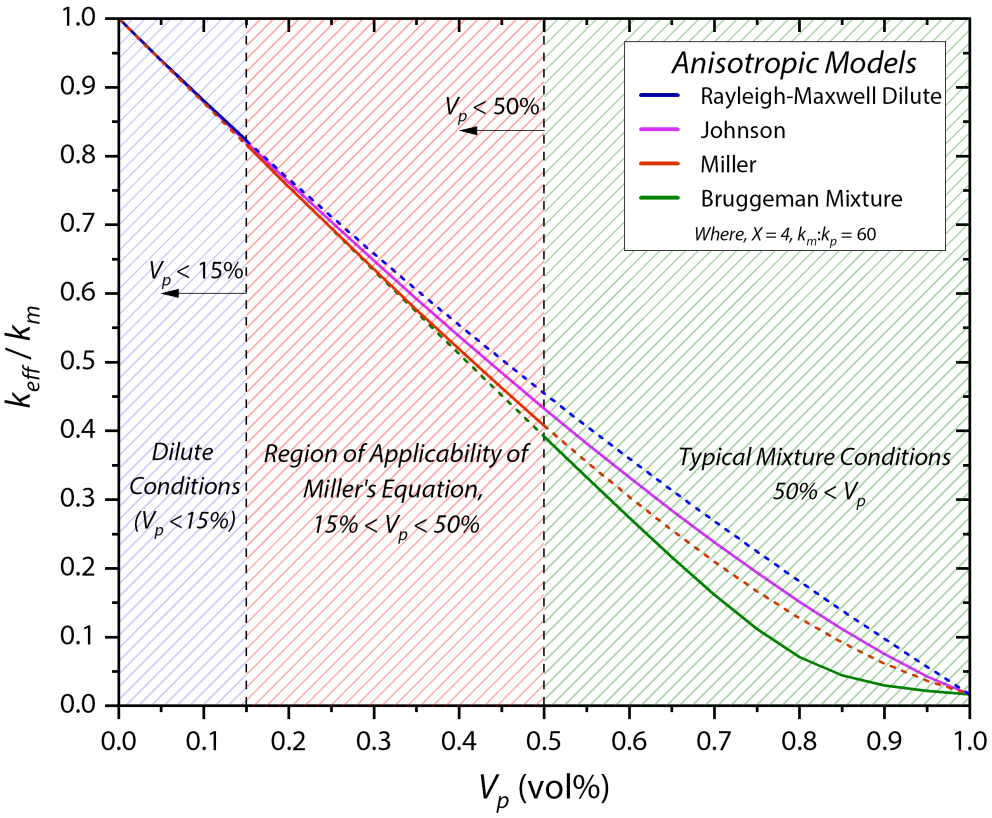

Figure 14. Comparison of anisotropic models in k_{eff}/k_m as a function of V_p. Depicts a material with a conductivity ratio k_m:k_p of 60, and with a geometric transformation of $X = 4$ [Equation (20)]. Areas of theoretical applicability are indicated as solid lines.

Table 2. Summary of conductivity models discussed in this paper.

Model	Model Type	Particle Shape	Particle Size	Limitations	Eqn.	Ref.
Maxwell-Rayleigh Dilute	Dispersion	Sphere	Mono-sized	V_p = 10-15% MAX	(15)	[108,109,111]
Bruggeman Variable	Dispersion	Sphere	Various	Needs large Δ in particle size	(16)	[112]
Meredith-Tobias Binary	Dispersion	Sphere	Two Sizes	$k_{eff} \neq k_p$ as $V_p \rightarrow 1.0$	(18)	[113]
Bruggeman Mixture	Mixture	Sphere	-	Requires a mixture ($V_p \approx 50\%$)	(19)	[112]
Maxwell-Rayleigh-Fricke	Dispersion	Ellipsoid	Mono-sized	V_p = 10-15% MAX	(21)	[108,109,114]
Miller	Dispersion	Ellipsoid	Various	Semi-empirical	(23)	[111]
Johnson	Dispersion	Ellipsoid	Various	-	(24)	[115]
Meredith-Tobias-Fricke	Dispersion	Ellipsoid	Two Sizes	$k_{eff} \neq k_p$ as $V_p \rightarrow 1.0$	-	[113,114]
Bruggeman-Fricke Mixture	Mixture	Ellipsoid	-	V_p = 50% MIN	(20)	[112,114]

4.1.3 *Experimental and Analytical Results*

Literature regarding the thermal conductivity of cermet materials is limited; however, some experimental data exists, particularly in the subfield of cermet nuclear fuels. Grossman experimentally

determined thermal conductivity values for W-UO_2 cermets by using a modified radial flow method and found that an ~80 vol.% (actual 75.9 vol.%) UO_2 specimen showed comparable results to analytical values approximated by the Bruggeman variable dispersion model Equation (16).[119] Miller applied the semi-empirical Miller model Equation (23) against LFA experimental data from UO_2 dispersions in tungsten ranging from V_p = 10-40 vol.%, and found that the method provided results within the experimental errors of the method used (10% for LFA).[111,120] The material contained particles that were distorted in a preferred orientation of the manufacturing process, and thus anisotropic ratios were estimated.[111] Le Flem et al.[121] determined thermal conductivities of Mo-TiC cermets ranging from 12.5-75 vol.% TiC from room temperature to 1000 °C with the LFA technique for use in structural applications of refractory material in the core of nuclear reactors. Jubin et al.[122] analyzed the thermophysical properties of the Oak Ridge National Laboratory (ORNL) cermet waste form discussed previously by performing SEM analysis of the phase boundaries, then determined an averaged overall thermal conductivity via micro heat transfer analysis of each of the individual phases. A detailed explanation of the process is provided in a recent publication by Almeida et al.,[123] who developed the technique.

4.2 Coefficient of Thermal Expansion

Additionally, for materials which contain multiple components, material stability is dependent on the coefficient of thermal expansion (CTE) mismatch that occurs between dissimilar materials. Examples pertaining to cermets, where the ceramic phase is encapsulated within the metallic phase are glass ceramics, where a crystalline phase is encapsulated by the glassy phase. Here a mismatch in CTE can produce highly anisotropic stresses at the crystal-glass interface causing accelerated interfacial corrosion.[124] In MMCs, Chawla et al.[125] found that thermal stresses generated in a single crystal copper matrix containing tungsten fibers produce higher dislocation densities around the fiber interface than in the bulk. The enhanced dislocation density and plastic deformation around the fiber is due to the CTE mismatch. Several investigations have attempted to model and control this behavior by controlling the ratio of metal to ceramic phases.[126] In particular, thermal stresses in a particulate composite may be calculated from the theory of elasticity, using Equation (25):

$$\frac{d^2u}{dr^2} + \frac{2}{r}\frac{du}{dr} - \frac{2}{r^2}u = 0 \tag{25}$$

Solving and applying boundary conditions, we find the stresses in the matrix (σ_{rm}) in polar coordinates, Equation (26). Where P is the interfacial pressure, V_p is the particle volume fraction, a is the particle radius, and r is the matrix radius. The full derivation is beyond the scope of this paper and is documented by Chawla,[127] as well as thermal stress distributions for fiber reinforced composites.

$$\sigma_{rm} = \frac{P}{1 - V_p}\left(\frac{a^3}{r^3} - V_P\right) \tag{26}$$

When designing a composite material as a radioactive waste form, it is desirable to minimize CTE mismatch between the ceramic or reinforcement phase and the metallic or binder phase while maintaining high thermal conductivity. Figure 15 illustrates the mismatch in CTE versus thermal conductivity for selected composites found in literature to guide the community on general composite material designs. In this plot, composites located in the lower-right quadrant are desirable and material discovery efforts should be expended to reveal as such. Composite compositions and references from Figure 15 are captured in Table S3 (Supporting Information).[128-141] Similar to thermal conductivity, it is also useful to model the coefficient of thermal expansion (CTE) for a given composite. Several models have been proposed to predict the CTE of the particle containing composites and are listed in Table 3, Where α_c is the linear CTE, V is the volume fraction, K is the bulk modulus, and G is the shear modulus. Subscripts c, p, and m represent the composite, particle, and matrix, respectively.

Table 3. Table listing several models to predict linear CTE.

Models	Expressions	Ref.
Rule of Mixtures (Voigt approximation)	$\alpha_c = V_m\alpha_m + V_p\alpha_p$	[142]
Turner's	$\alpha_c = \frac{\alpha_m V_m K_m + \alpha_p V_p K_p}{V_m K_m + V_p K_p}$	[143]
Kerner's	$\alpha_c = (1 - V_p)\alpha_m + V_p\alpha_p + \frac{V_p(1 - V_p)(\alpha_p - \alpha_m)(K_p - K_m)}{(1 - V_p)K_m + V_p K_p + 3K_p K_m/4G_m}$	[144]

While the above analytical models are dependent on the volume fraction and modulus, the CTE can also be tailored by adjusting the ratio of coarse to fine particle sizes.[128] Standard particle size definitions and terminology for Discontinuous Reinforced MMCs (DRMMCs) are provided in reference.[145]

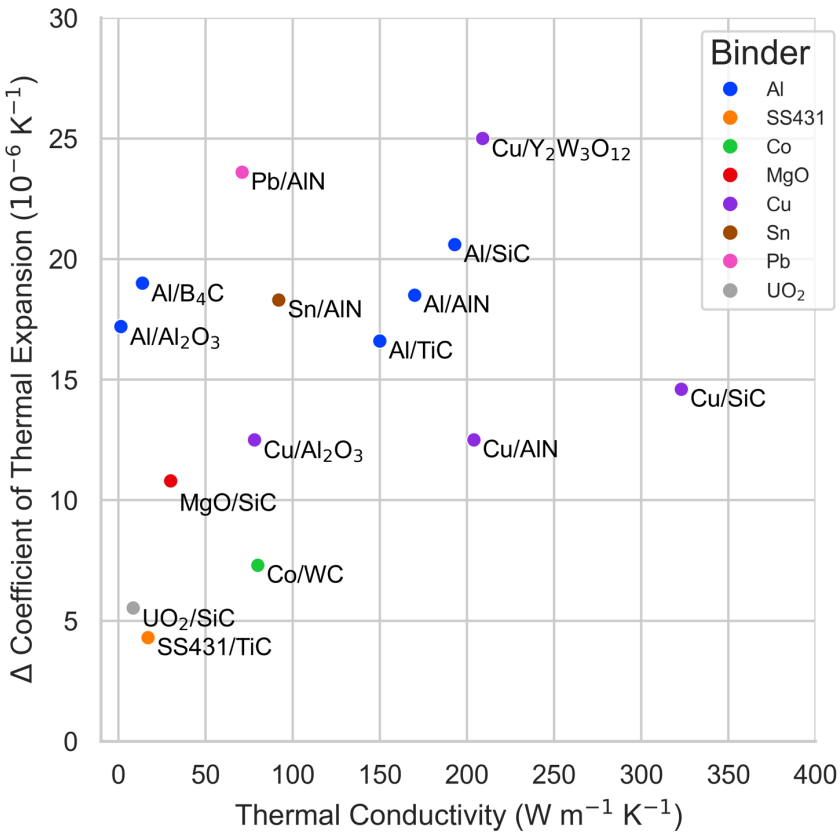

Figure 15. Plot of thermal conductivity vs. CTE mismatch for select composite materials found in literature. Several CMC are plotted for comparison. The legend and color palette indicate the binder phase or majority phase of each composite for comparison. Composite data are detailed in Table S3 (Supporting Information).

4.3 Chemical Durability

Although investigations do not exist for chemical durability testing of cermet radioactive waste forms, the chemical durability of vitrified waste forms to immobilize radioactive waste has been extensively studied.[21,146,147] These tests use standardized and internationally recognized testing protocols such as ASTM standards. Typical methods for evaluating chemical durability, in regard to release of key components (fission products or simulants) from a solidified waste form are ASTM C1220,[148] ASTM C1285-21,[149] and ASTM C1308[150] as well as others summarized in more detail by Thorpe et al.[151] The ASTM C1308 procedure could be used to qualify release of contaminants from a solidified waste form; however, ASTM C1285-21 is specific to glass waste forms. The ASTM C1220 method is commonly employed for studying

multiphase waste forms. While some of these tests use sieved particles and others use monoliths, preparing cermet-type materials for particle-type testing would be far more difficult than preparing glasses or ceramics without metal phases. Thus, it seems practical that a new type of testing protocol be developed for evaluating leaching behavior for cermet-type materials. Additionally, studies investigating corrosion of MMCs can be of use.[152-158]

MMC corrosion studies of metal matrix composites are discussed and summarized in Table S4 (Supporting Information).[152-157,159] It should be noted that various methods, conditions, and units are reported in different chemical durability and corrosion studies. Common chemical durability tests for nuclear waste forms are generally performed using different types of product consistency tests (PCT), as previously discussed, whereas the methods of corrosion tests include Tafel polarization technique (TPT), zero resistance ammeter (ZRA), and mixed-potential theory.[160] The result of chemical durability test is reported in mass/area/time (i.e., g m^{-2} d^{-1} and g cm^{-2} min^{-1}), and corrosion rate testing is generally given as a penetration rate in the units of length $time^{-1}$ (e.g., mil $year^{-1}$, cm $year^{-1}$) or mass loss over time.

Shanbhag et al.[152] investigated the corrosion behavior of Al 7075 alloy reinforced with 10 or 15 mass% of Al_2O_3 using the simulant solutions of sea water (3.5 mass% NaCl) and industrial environment [$NaCl + (NH_4)_2SO_4$] at room temperature. The Al 7075 alloy is composed of ~88 mass% Al, 5.1-6.1 mass% Zn, 2.1-2.9 mass% Mg, 1.2-2 mass% Cu, 0.3 mass% Mn, 0.5 mass% Fe, 0.4 mass% Si, 0.3 mass% Mn, 0.2-0.3 mass% Cr, and 0.1 mass% Ti. The Al 7075/Al_2O_3 MMC was fabricated by stir casting method. The result of corrosion test showed pitting corrosion in seawater and intergranular corrosion in industrial environment. Increasing Al_2O_3 content in Al 7075 increased the corrosion rate in both solutions of sea water and industrial environment. The authors suggest that the increase in corrosion rate was due to the formation of brittle intermetallic phases at the matrix/particle interface, which reduced interfacial bonding and increased porosity.

Tandler et al.[153] studied the effects on corrosion behavior of adding SiC particles to an $AlSi_7Mg$ alloy. The Al alloy contained 7.2 mass% Si and <1 mass% of other elements including Fe, Cu, Mg, Ni, Ti, and Mn. The samples of $AlSi_7Mg$/SiC MMC were extruded or heat treated (protocol T6) before corrosion

testing. Corrosion testing was performed in either wet air atmosphere or sea water simulant solution at 22 ℃. The results showed that addition of SiC to Al alloy increased the corrosion rates in both wet air atmosphere or sea water simulant solution, and the corrosion rate was lower for the heat-treated samples compared to heat treated samples.

Vasudevan et al.[154] studied the corrosion behavior of AA 5083 aluminum alloy reinforced with 7, 9, or 10 mass% of B_4C particles. The AA 5083 aluminum alloy contained 4-4.9 mass% of Mg and ~1.3 mass% of other elements including Si, Fe, Cu, Mn, Zn, Ti, and Cr. The corrosion test was performed with salt spray method (ASTM B117) using 5 mass% NaCl solution in air at 35℃. Results showed that increasing B_4C content increased the corrosion rate of AA 5083/B_4C MMC.

Sherif et al.[155] investigated the effect of graphite (Gr) on the corrosion behavior of Al/Gr composite by varying 0-3 mass% of graphite. The corrosion test was performed using 3.5 mass% NaCl solution at room temperature, and potentiodynamic polarization data was used to evaluate corrosion parameters. The results showed that increasing graphite content in the Al/Gr composite increased the corrosion rate. The graphite particles could be cathodic relative to the Al matrix and lead to galvanic corrosion.

Hihara and Kondepudi[156] performed corrosion tests on a ZE 41A Mg/SiC MMC. The composition of ZE41A Mg alloy is 93.9 mass% Mg, 4.2 mass% Zn, 0.7 mass% Zr, and 1.2 mass% of rare-earth elements, and the SiC monofilament was used. The corrosion test was performed using oxygenated or de-aerated 0.5 M $NaNO_3$ solution at 30 ℃ and 1 atm. Addition of SiC increased corrosion rate of MMC, and the corrosion rate of MMC was higher in oxygenated solution compared to de-aerated solution.

Jaiswal et al.[157] developed a Mg alloy reinforced with hydroxyapatite (HA) [$Ca_{10}(PO_4)_6(OH)_2$] to improve the corrosion resistance. The Mg alloy contained 3 mass% Zn, and 0, 2, 5, or 10 mass% of HA was added to the MMC for corrosion testing. Potentiodynamic polarization data was used to calculate corrosion parameters. Addition of 5 mass% HA to MMC resulted in the lowest corrosion rate and reduced the corrosion rate by 42% compared to the original Mg alloy. The authors mentioned that higher corrosion rate on the MMC with 10 mass% HA compared to 5 mass% sample was due to the detachment of the apatite layer from the surface of composites.

Stüpp et al.[159] investigated the corrosion behavior of a ZK60/HA MMC for biomedical applications. The ZK60 alloy contains 93.4 mass% Mg, 6 mass% Zn, and 0.6 mass% Zr. The corrosion test was performed on ZK60/HA MMC samples with 0-20 mass% HA using the simulant solution of physiological conditions. The result showed that increasing HA content decreased the corrosion rate.

5 Cermets as Radioactive Waste Forms

For the reasons discussed herein, cermets are excellent candidates for radiological waste forms. The use of cermet materials for radioactive waste form applications has been explored for their high waste load capacity, and high thermal conductivities. Table 4, provides a summary of cermets produced to immobilize radiological waste. In a study by Oak Ridge National Laboratory (ORNL), calcined products of a waste simulant comprised of 1-2 μm sized particles were mixed with several metals (Ni, Cu, Mo, Al, Si) and were hot pressed into pellets at 4000 pounds per square inch (PSI) for 1 hour at 1050 °C to 1100 °C.[5] Various metal compositions and metal:oxide ratios were included in the study, most notably a metal alloy comprised of 70% Fe, 20% Ni, 5% Cu, and 5% Mo (by mass) with an oxide loading of 27.5%.[5] The author described this particular composition of having similar thermal conductivities to pure Hastelloy series metal alloys.[5] The large quantities of reducible metal oxides in the waste precursor presents a key advantage for the cermet waste form. The high actual waste loading of this composition was greatly aided by the ability to reduce these species, particularly iron oxides, under hydrogen back to their metallic form prior to densification.[5] This saved on non-contaminated material cost and in turn produced a thermally conductive, dense cermet (7.35 g cm^{-3}) with a high waste loading of approximately 75 mass%, which amounts to a volume reduction of 200:1 or a mass concentration ratio of 100:1.[5]

In another study by Argonne National Laboratory, cermet waste forms were explored for their advantages in thermal conductivity, particularly to encapsulate radioisotopes that generate a large amount of heat such as ^{137}Cs and ^{90}Sr.[6] Ortega et al.[6] also observed the incorporation of molybdenum into the final form as this and other fission products (e.g., noble metals) typically exhibit low solubility in glass waste forms. The metal utilized in these experiments was a bronze alloy (10 mass% Sn in Cu). This was chosen for its low melting temperature to avoid the possible volatilization of the lighter elements and due to the

inert nature of this alloy. Unlike the study by Aaron et al.,[5] which utilized calcined waste products as the ceramic phase, this study elected for a cold-press-and-sinter approach to produce a separate preformed ceramic waste form prior to the addition of the metal matrix. This preformed ceramic was created by adding a dissolved simulated waste stream containing nitrate salts with sodium bentonite, which formed alkali and alkaline earth aluminosilicates and aided in the reduction of cesium. This dense ceramic was then crushed, mixed with the bronze powder and molybdenum carbide, and then was cold pressed to 300 MPa and sintered at 600°C to 800 °C under hydrogen. The result of a 30:70 mass% oxide:metal ratio yielded a cermet with a continuous metallic bronze matrix, which exhibited a much higher thermal conductivity than that of the more porous specimens. In addition, elemental distributional analysis with energy dispersive X-ray spectroscopy (EDS) illustrated no noticeable chemical reactions between the metallic and ceramic phases and showed that the volatile compounds were contained within the aluminosilicate material, theoretically preventing those compounds from being released in the case of corrosion to the metal phase.

Development of cermet waste forms to immobilize high-heat-generating components including ^{137}Cs/Ba and ^{90}Sr/Y, residual fission products from the solvent extraction process, and undissolved noble metals were reported by Jubin et al.[122] For the metal matrix of the cermet waste form, mixtures of the undissolved solid simulant (Mo, Re, Ru, Rh, Pd) and hardware waste simulant (Fe, Cr, Ni, Sn, and SnO_2) in different mass% ratios were used for the study. For the ceramic components, surrogate waste solution to simulate the components (i.e., Zr, Mo, La, Ce, Pr, Nd, Sm, Eu, Gd, Cs, Ba, Rb, Sr) of Dresden SNF reprocessing was used. The mass ratio of metal:ceramic components was 75:25. The micro-heat-transfer analysis showed that the synthesized cermet waste forms were nearly orthotropic. Thermal conductivity measurements were performed on one sample, and the area-averaged thermal conductivity of 49 W m^{-1} K^{-1} was reported. Overall, the study demonstrated the successful synthesis of a cermet composed of only the intrinsic waste components from the SNF reprocess and hardware waste.

Crum et al.[93] investigated the cermet waste form of ε-metal (an alloy of five metals including Mo, Pd, Rh, Ru, and Tc), which is found within SNF, using three different synthesis methods where Tc was replaced with Re as the surrogate. The compositions of cermet waste forms were 82.5% or 65% (by mass)

of ε-metals with 17.5% or 35% of ZrO_2. For the consolidation processes, SPS, HIP, and microwave sintering (MS) methods were used. The presence of ZrO_2 improved the formation of the epsilon phase in SPS process but hindered the consolidation in MS process. Most of the porosity was in the grain boundaries of ZrO_2, possibly due to the phase transition from cubic to monoclinic phase during cooling from high temperature, which could be overcome by stabilizing the ZrO_2 in the cubic structure with minor additions. This study demonstrated that SPS and HIP processes can be used to produce dense cermet waste forms of epsilon metals.

Table 4. Development of cermets for nuclear waste forms in literature. *Ceramic elements were present as oxides.

Metal elements	Ceramic elements*	Metal:ceramic ratio (mass%)	Ref.
Fe, Ni, Cu, Mo	Fe, Mn, Al, Ce, Zr, Sr, U, Ru, Cs, Sm, Na	72.5:27.5	[5]
Fe, Ni	La, Ce, Cs, Sr, Ru, Zr, U, Fe, Ni, Cr, Na	80:20, 70:30, 60:40	[5]
Cu	Al, U, C, U, Pu, Stainless Steel	NA	[161]
Fe, Cr, Ni, Sn, Mo, Re, Ru, Rh, Pd	Zr, Mo, La, Ce, Pr, Nd, Sm, Eu, Gd, Cs, Ba, Rb, Sr	75:25:00	[122]
Fe, Cr, Ni, Sn, Mo, Re, Ru, Rh, Pd	Ce	75:25:00	[122]
Cu, Sn	Cs, Sr, Rb, Ba, bentonite clay	70:30, 50:50	[6]
Cu, Sn	Mo_2C, Cs, Sr, Rb, Ba, bentonite clay	50:50:00	[6]
Mo, Pd, Re, Rh, Ru, Tc	Zr	65:35, 82.5:17.5	[93]

6 Contemporary Perspective on Cermets

In October 2023 a workshop was hosted at Argonne National Laboratory by the U.S. Department of Energy – Office of Nuclear Energy on the historical testing of cermets within the US programs, current state-of-the-art in cermet materials and R&D needs moving into the future. The workshop involved representatives from industry, academia and national laboratories from the U.S., United Kingdom, Canada, Australia and South Korea. Topics included the overall fit of cermets into different global waste management strategies, selection criteria for matrix design, the design and processing of cermets, waste form conversions, corrosion behavior, and modeling. A full summary of the workshop is available elsewhere.[162] There were several common themes running through the workshop that highlight the current

community perception of cermets in the waste disposal community. Several of these topics have been summarized at length in this review. The general agreement among workshop participants was that cermets are a critical addition for the long-term strategy for immobilizing radioactive waste. However, relying solely on historical and sporadic efforts is inadequate to advance the technology in response to evolving needs and opportunities. The main hurdles that could hinder development of cermets were; a lack of baseline waste stream(s) for cermet development to improve comparisons of material performance; the need to define what a baseline cermet performance should require in terms of processing controls and waste form durability; the lack of a standardized test or suite of tests to adequately assess and compare cermet corrosion behavior; a lack of focus on scale-up related-properties of radiological fabrication processes; and limited interactions between industries involved in cermets. The outlook for cermets remains highly positive and is clear that engagement from across the waste form community will be required to eliminate the hurdles to their maturation to meet current and emerging waste disposal challenges.

7 Summary and Conclusions

Composite materials containing metals and ceramics are referred to by different names in the literature including *metal matrix composites* (MMC), *ceramic matrix composites* (CMC), *cermets*, and *hard metals*. Flexibility in cermet design offers opportunities to tailor waste forms which are suitable for a variety of waste streams, including legacy waste, LWR SNF, and future AR waste. While cermets should not be considered the “holy-grail” of radioactive waste forms, they will play a critical role in arenas where other waste forms underperform, such as residual halides, noble metals and high-heat producing radioisotope immobilization. Applications where cermet materials are documented in literature include hardening tools, nuclear thermal propulsion, and nuclear waste forms, where the focus of this paper is on the latter. These types of composite materials can be produced using a variety of techniques including powder processing, pressureless sintering, liquid phase sintering, in-situ processing, ultrafast high-temperature sintering, mechanical milling, as well as hot-pressing techniques such as hot uniaxial pressing (including spark plasma sintering) and hot isostatic pressing. While hot pressing provides significant benefits in terms of densification (removal of porosity) of the composite form and allows for particle-particle sintering to occur,

performing hot pressing on nuclear materials has added safety challenges. To address safety issues, concepts such as encapsulation of the MMC using a metal as the encapsulant (enveloping) phase provides a depth-in-defense strategy where surface degradation of the waste form will not leach radioisotopes. Additionally, the metallic phase provides a significant increase in thermal conductivity of the overall composite due to the high conductivity of the metallic phase, which allows other properties such as malleability, chemical durability, and waste loading to be appropriately tailored. The increased thermal conductivity allows these metal-containing composites to achieve much higher fission product loadings than the more traditional-type waste forms (e.g., glasses, ceramics). During processing, temperatures well below the melting temperature of the metallic phase can be maintained reducing material volatilization. Examples of cermet-type waste forms are provided and discussed in more detail. Overall, this type of nuclear waste immobilization strategy shows great promise for a variety of nuclear waste applications.

8 Funding Details

This work was funded by the Department of Energy Office of Nuclear Energy (DOE-NE) under the Material Recovery and Waste Form Development (MRWFD) Campaign. Authors thank Ken Marsden (Idaho National Laboratory), Kimberly Gray (DOE-NE), and Ming Tang (DOE-NE) for their support. This paper was prepared to support the U.S. DOE Cermet Waste Forms for Nuclear Fuel Cycle Technologies Workshop. JE and JM report partial funding support by ARPAe, under contract DE-AT0001614.

9 Disclosure Statement

No potential conflict of interest was reported by the authors.

10 Author Information

Corresponding Authors

Jonathan S. Evarts - *Pacific Northwest National Laboratory, Richland, WA 99354, USA;* ORCiD orcid.org/0000-0002-2991-0396; email: jonathan.evarts@pnnl.gov

Brian J. Riley - *Pacific Northwest National Laboratory, Richland, WA 99354, USA;* ORCiD orcid.org/0000-0002-7745-6730F; email: brian.riley@pnnl.gov

John *S. McCloy - School of Mechanical and Materials Engineering, Washington State University, Pullman, WA 99164, USA;* ORCiD orcid.org/0000-0001-7476-7771; email: john.mccloy@wsu.edu

Authors

Saehwa Chong – *Pacific Northwest National Laboratory, Richland, WA 99354, USA;* ORCiD orcid.org/0000-0002-4722-0022

Jared M. Oshiro - *Pacific Northwest National Laboratory, Richland, WA 99354, USA;* ORCiD orcid.org/0009-0001-4294-9690

R. Matthew Asmussen - *Pacific Northwest National Laboratory, Richland, WA 99354, USA;* ORCiD orcid.org/0000-0001-5977-7728

11 Supporting Information

Supporting information is available free of charge at https://pubs.acs.org

Volatile off-gas waste components and methods for immobilization; spent fuel compositions for various fuel cycle schemes; summary of chemical durability and corrosion test data for selected cermets; Figure 15 data for MMC and CMC compositions including thermal conductivity and CTE for each phase.

12 Acknowledgements

Pacific Northwest National Laboratory (PNNL) is operated by Battelle Memorial Institute for the DOE under contract DE-AC05-76RL01830. Authors thank Ewan Maddrell (National Nuclear Laboratory, NNL) for providing some of the graphics and for helpful conversations with Josh Turner (NNL) and Krista Carlson (University of Nevada Reno). This work was funded by the Department of Energy Office of Nuclear Energy (DOE-NE) under the Material Recovery and Waste Form Development (MRWFD) Campaign. Authors thank Ken Marsden (Idaho National Laboratory), Kimberly Gray (DOE-NE), and Ming Tang (DOE-NE) for their support. During the preparation of this work, the authors used Microsoft Bing Image Creator to develop portions of Figure 1. After using this tool/service, the authors reviewed and edited the content as needed and take full responsibility for the content of the publication.

13 References

(1) Kübarsepp, J.; Juhani, K. Cermets with Fe-alloy binder: A review. **2020**, *92*, 105290.

(2) Kubarsepp, J.; Juhani, K.; Tarraste, M. Abrasion and Erosion Resistance of Cermets: A Review. **2021**, *15*.

(3) Johnson, J. A.; Wilkerson, R. P.; Williams, J. K.; Thompson, G. B. Grain size control by matrix phase additives in nuclear thermal propulsion cermets. *J. Nucl. Mater.* **2023**, *577*, 154306.

(4) Haertling, C.; Hanrahan Jr, R. Literature review of thermal and radiation performance parameters for high-temperature, uranium dioxide fueled cermet materials. *J. Nucl. Mater.* **2007**, *366*, 317.

(5) Aaron, W.; Quinby, T.; Kobisk, E. *Cermet High Level Waste Forms*, ORNL/TM-6404, Oak Ridge National Laboratory, Oak Ridge, TN, 1978.

(6) Ortega, L.; Zeng, Z.; Kaminski, M.; Cunnane, J.; Natesan, K. Cermet waste forms for waste streams from advanced aqueous processing of spent nuclear fuels-11348. In Proc. Waste Management 2011.

(7) Ortega, L. H.; Kaminski, M. D.; Zeng, Z.; Cunnane, J. Nuclear fuel cycle waste stream immobilization with cermets for improved thermal properties and waste consolidation. *J. Nucl. Mater.* **2013**, *438*, 126.

(8) Stewart, M. W.; Moricca, S. A.; Eddowes, T.; Zhang, Y.; Vance, E. R.; Lumpkin, G. R.; Carter, M. L.; Dowson, M.; James, M. The use of Hot-Isostatic Pressing to process nuclear waste forms. In Proc. International Conference on Radioactive Waste Management and Environmental Remediation. Vol. 44076 p611.

(9) Mari, D., *Cermets and Hardmetals*, In *Encyclopedia of Materials: Science and Technology*; Buschow, K. H. J., Cahn, R. W., Flemings, M. C., Ilschner, B., Kramer, E. J., Mahajan, S., Veyssière, P., Eds.; Elsevier Ltd.: Oxford, 2001, p 1118.

(10) Ettmayer, P. Hardmetals and Cermets. *Annual Rev. Mater. Sci.* **1989**, *19*, 145.

(11) IAEA *Status and Trends in Spent Fuel and Radioactive Waste Management*; International Atomic Energy Agency: Vienna, Austria, 2018.

(12) Donald, I. W. *Waste Immobilization in Glass and Ceramic Based Hosts: Radioactive, Toxic and Hazardous Wastes*; John Wiley & Sons, 2010.

(13) McDaniel, E.; Terry, J. *Immobilization of chloride-rich radioactive wastes produced by pyrochemical operations*, ORNL/TM-13486, Oak Ridge National Laboratory, Oak Ridge, TN, 1997.

(14) Hrma, P. R. *Retention of Halogens in Waste Glass*, PNNL-19361, Pacific Northwest National Laboratory, Richland, WA, 2010.

(15) Riley, B. J.; Rieck, B. T.; McCloy, J. S.; Crum, J. V.; Sundaram, S.; Vienna, J. D. Tellurite glass as a waste form for mixed alkali–chloride waste streams: Candidate materials selection and initial testing. *J. Nucl. Mater.* **2012**, *424*, 29.

(16) Riley, B. J.; Schweiger, M. J.; Kim, D.-S.; Lukens Jr, W. W.; Williams, B. D.; Iovin, C.; Rodriguez, C. P.; Overman, N. R.; Bowden, M. E.; Dixon, D. R. Iodine solubility in a low-activity waste borosilicate glass at 1000°C. *J. Nucl. Mater.* **2014**, *452*, 178.

(17) Ojovan, M. I.; Lee, W. E.; Kalmykov, S. N. *An Introduction to Nuclear Waste Immobilisation (Third Edition)*; Elsevier Ltd.: Amsterdam, Netherlands, 2019.

(18) Goel, A.; McCloy, J. S.; Fox, K. M.; Leslie, C. J.; Riley, B. J.; Rodriguez, C. P.; Schweiger, M. J. Structural analysis of some sodium and alumina rich high-level nuclear waste glasses. *J. Non-Cryst. Solids* **2012**, *358*, 674.

(19) Colburn, H. A.; Peterson, R. A. A history of Hanford tank waste, implications for waste treatment, and disposal. *Environ. Prog. Sustain. Energy* **2020**, *40*, e13567.

(20) Marcial, J.; Riley, B. J.; Kruger, A. A.; Lonergan, C. E.; Vienna, J. D. Hanford low-activity waste vitrification: A review. *J. Haz. Mater.* **2023**, *461*, 132437.

(21) Goel, A.; McCloy, J. S.; Pokorny, R.; Kruger, A. A. Challenges with vitrification of Hanford high-level waste (HLW) to borosilicate glass–An overview. *J. Non-Cryst. Solids X* **2019**, *4*, 100033.

(22) Ojovan, M. I.; Lee, W. E.; Kalmykov, S. N. *An introduction to nuclear waste immobilisation*; Elsevier, 2019.

(23) Riley, B. J.; McFarlane, J.; DelCul, G. D.; Vienna, J. D.; Contescu, C. I.; Forsberg, C. W. Molten salt reactor waste and effluent management strategies: A review. *Nucl. Eng. Des.* **2019**, *345*, 94.

(24) Smith, G. P. *Corrosion of Materials in Fused Hydroxides*, ORNL-2048, Oak Ridge National Laboratory, Oak Ridge, TN, 1956.

(25) IAEA *Design of Off-Gas and Air Cleaning Systems at Nuclear Power Plants*; International Atomic Energy Agency: Vienna, Austria, 1987; Vol. Technical Report Series 274 (STI/DOC/010/274).

(26) Greenwood, M. S.; Betzler, B.; Flanagan, G.; Holcomb, D.; Qualls, A. L.; Worrall, A. *Thermal-fluoride and fast-chloride molten salt-fueld reactor dynamic models for licensing, safeguards, and separations investigations*, ORNL/TM-2018/XXX, Oak Ridge National Laboratory, Oak Ridge, TN, 2018.

(27) Zagnit'ko, A. V.; Chuvilin, Y. D. Nanoaerosols formation during the bubbling of lithium and beryllium fluorides molten salt to produce reactor radioisotopes. *Nanotech. Russia* **2009**, *4*, 851.

(28) Vienna, J. D.; Collins, E. D.; Crum, J. V.; Ebert, W. L.; Frank, S. M.; Garn, T. G.; Gombert, D.; Jones, R.; Jubin, R. T.; Maio, V. C.; Marra, J. C.; Matyas, J.; Nenoff, T. M.; Riley, B. J.; Sevigny, G. J.; Soelberg, N. R.; Strachan, D. M.; Thallapally, P. K.; Westsik, J. H. *Closed Fuel Cycle Waste Treatment Strategy*, FCRD-MRWFD-2015-000674, PNNL-24114, Pacific Northwest National Laboratory, Richland, WA, 2015.

(29) Bruffey, S. H.; Jubin, R. T.; Jordan, J. A. Capture of Elemental and Organic Iodine from Dilute Gas Streams by Silver-exchanged Mordenite. *Procedia Chem.* **2016**, *21*, 293.

(30) Matyáš, J.; Fryxell, G. E.; Busche, B. J.; Wallace, K.; Fifield, L. S. Functionalized silica aerogels: Advanced materials to capture and immobilize radioactive iodine. In Proc. Ceramic Materials for Energy Applications: Ceramic Engineering and Science. **2011**; Vol. 32 p23.

(31) Riley, B. J.; Kroll, J. O.; Peterson, J. A.; Matyáš, J.; Olszta, M. J.; Li, X.; Vienna, J. D. Silver-loaded aluminosilicate aerogels as iodine sorbents. *ACS Appl. Mater. Interfaces* **2017**, *9*, 32907.

(32) Riley, B. J.; Chun, J.; Um, W.; Lepry, W. C.; Matyáš, J.; Olszta, M. J.; Li, X.; Polychronopoulou, K.; Kanatzidis, M. G. Chalcogen-based aerogels as sorbents for radionuclide remediation. *Environ. Sci. Technol.* **2013**, *47*, 7540.

(33) Riley, B. J.; Pierce, D. A.; Lepry, W. C.; Kroll, J. O.; Chun, J.; Subrahmanyam, K. S.; Kanatzidis, M. G.; Alblouwy, F. K.; Bulbule, A.; Sabolsky, E. M. Consolidation of tin sulfide chalcogels and xerogels with and without adsorbed iodine. *Ind. Eng. Chem. Res.* **2015**, *54*, 11259.

(34) Hao, Y.; Tian, Z.; Liu, C.; Xiao, C. Recent advances in the removal of radioactive iodine by bismuth-based materials. *Front. Chem.* **2023**, *11*, 1122484.

(35) Asmussen, R.; Turner, J.; Chong, S.; Riley, B. J. Review of recent developments in iodine wasteform production. *Front. Chem.* **2022**, *10*, 1043653.

(36) Tesfay Reda, A.; Pan, M.; Zhang, D.; Xu, X. Bismuth-based materials for iodine capture and storage: A review. **2021**, *9*, 105279.

(37) Baker, F. S.; Contescu, C. I.; Tsouris, C.; McFarlane, J. *Activated Carbon Composites for Air Separation*, ORNL/TM-2007/329, Oak Ridge National Laboratory, Oak Ridge, TN, 2007.

(38) Liu, J.; Fernandez, C. A.; Martin, P. F.; Thallapally, P. K.; Strachan, D. M. A two-column method for the separation of Kr and Xe from process off-gases. *Ind. Eng. Chem. Res.* **2014**, *53*, 12893.

(39) Subrahmanyam, K. S.; Spanopoulos, I.; Chun, J.; Riley, B. J.; Thallapally, P. K.; Trikalitis, P. N.; Kanatzidis, M. G. Chalcogenide aerogels as sorbents for noble gases (Xe, Kr). *ACS Appl. Mater. Interfaces* **2017**, *9*, 33389.

(40) Salvatores, M.; Palmiotti, G. Radioactive waste partitioning and transmutation within advanced fuel cycles: Achievements and challenges. *Prog. Part. Nucl. Phys.* **2011**, *66*, 144.

(41) OECD *Advanced Nuclear Fuel Cycles and Radioactive Waste Management*, NEA-5990, Nuclear Energy Agency - Organisation for Economic Co-operation and Development, Paris, France, 2006.

(42) Nagarajan, K.; Reddy, B. P.; Ghosh, S.; Ravisankar, G.; Mohandas, K. S.; Mudali, U. K.; Kutty, K. V. G.; Viswanathan, K. V. K.; Babu, C. A.; Kalyanasundaram, P.; Rao, P. R. V.; Raj, B. Development of Pyrochemical Reprocessing for Spent Metal Fuels. *Energy Procedia* **2011**, *7*, 431.

(43) Geist, A.; Adnet, J.-M.; Bourg, S.; Ekberg, C.; Galán, H.; Guilbaud, P.; Miguirditchian, M.; Modolo, G.; Rhodes, C.; Taylor, R. An overview of solvent extraction processes developed in Europe for advanced nuclear fuel recycling, part 1—Heterogeneous recycling. **2021**, *56*.

(44) Lyseid Authen, T.; Adnet, J.-M.; Bourg, S.; Carrott, M.; Ekberg, C.; Galán, H.; Geist, A.; Guilbaud, P.; Miguirditchian, M.; Modolo, G.; Rhodes, C.; Wilden, A.; Taylor, R. An overview of solvent extraction processes developed in Europe for advanced nuclear fuel recycling, Part 2 — homogeneous recycling. *Separ. Sci. Technol.* **2021**, *57*, 1724.

(45) McCloy, J. S.; Schuller, S. Vitrification of wastes: From unwanted to controlled crystallization, A review. *Compt. Rend. Geosci.* **2022**, *354*, 1.

(46) Mussatto, A.; Ahad, I. U. I.; Mousavian, R. T.; Delaure, Y.; Brabazon, D. Advanced production routes for metal matrix composites. *Eng. Rep.* **2020**, *3*, e12330.

(47) Parikh, V. K.; Patel, V.; Pandya, D. P.; Andersson, J. Current status on manufacturing routes to produce metal matrix composites: State-of-the-art. *Heliyon* **2023**, *9*, e13558.

(48) Chaira, D., *Powder Metallurgy Routes for Composite Materials Production*, In *Encyclopedia of Materials: Composites*; Elsevier Inc.: Amsterdam, The Netherlands, 2021, p 588.

(49) Mussatto, A.; Ahad, I. U. I.; Mousavian, R. T.; Delaure, Y.; Brabazon, D. Advanced production routes for metal matrix composites. **2020**, *3*.

(50) Guo, M.; Dong, Q.; Xie, H.; Wang, C.; Zhao, Y.; Wang, X.; Zhong, W.; Li, Z.; Wang, R.; Wang, Y.; Hao, L.; He, S.; Chen, G.; Xiong, W.; Zhao, J.-C.; Hu, L. Ultrafast high-temperature sintering to avoid metal loss toward high-performance and scalable cermets. *Matter* **2022**, *5*, 594.

(51) German, R. M.; Suri, P.; Park, S. J. Review: liquid phase sintering. *J. Mater. Sci.* **2009**, *44*, 1.

(52) Maddrell, E.; Vance, E.; Gregg, D. Capture of iodine from the vapour phase and immobilisation as sodalite. *J. Nucl. Mater.* **2015**, *467*, 271.

(53) Riley, B. J. Electrochemical Salt Wasteform Development: A Review of Salt Treatment and Immobilization Options. *Ind. Eng. Chem. Res.* **2020**, *59*, 9760.

(54) Yadav, A.; Chong, S.; Riley, B. J.; McCloy, J. S.; Goel, A. Iodine Capture by Ag-Loaded Solid Sorbents Followed by Ag Recycling and Iodine Immobilization: An End-to-End Process. *Ind. Eng. Chem. Res.* **2023**, *62*, 3635.

(55) Riley, B. J.; Vienna, J. D.; Strachan, D. M.; McCloy, J. S.; Jerden, J. L. Materials and processes for the effective capture and immobilization of radioiodine: A review. *J. Nucl. Mater.* **2016**, *470*, 307.

(56) Riley, B. J.; Chong, S. "Iodine Capture and Encapsulation," U.S. patent#: 63/596,781 patent application#: 63/596,781, 2023.

(57) Holladay, D. W. *A literature survey: Methods for the removal of iodine species from off-gases and liquid waste streams of nuclear power and nuclear fuel reprocessing plants, with emphasis on solid sorbents*, ORNL/TM-6350, Oak Ridge National Laboratory, Oak Ridge, TN, 1979.

(58) Bruffey, S. H.; Jubin, R. T.; Jordan, J. A. *Fundamental Aspects of Zeolite Waste Form Production by Hot Isostatic Pressing*, FCRD-MRWFD-2016-000267, ORNL/SR-2016/759, Oak Ridge National Laboratory, Oak Ridge, TN, 2016.

(59) Bruffey, S. H.; Jordan, J. A.; Jubin, R. T.; Parks, M. L.; Watkins, T. R. *Hot Isostatic Pressing of Engineered Forms of I-AgZ*, ORNL/SR-2017/707, NTRD-MRWFD-2017-000412, Oak Ridge National Laboratory, Oak Ridge, TN, 2017.

(60) Bruffey, S. H.; Jubin, R. T. *Preparation of Four Large-format Hot Isostatically Pressed I-AgZ Waste Form Samples for Performance Testing*, NTRD-MRWFD-2018-000198; ORNL/SPR-2018/1026, Oak Ridge National Laboratory, Oak Ridge, TN 2018.

(61) Jubin, R.; Bruffey, S.; Patton, K. *Expanded Analysis of Hot Isostatic Pressed Iodine-Loaded Silver-Exchanged Mordenite*, FCRD-SWF-2014-000278; ORNL/LTR-2014/476, Oak Ridge National Laboratory, Oak Ridge, TN, 2014.

(62) Maddrell, E.; Vance, E.; Grant, C.; Aly, Z.; Stopic, A.; Palmer, T.; Harrison, J.; Gregg, D. Silver iodide sodalite–Wasteform/HIP canister interactions and aqueous durability. *J. Nucl. Mater.* **2019**, *517*, 71.

(63) Maddrell, E. R. *The Immobilisation of Mercury Containing Residues*, NNL(11)-11805, National Nuclear Laboratory, Sellafield, Cumbria, United Kingdom, 2012.

(64) Reshetnyak, H.; Kuybarsepp, J. Mechanical properties of hard metals and their erosive wear resistance. *Wear* **1994**, *177*, 185.

(65) Figiel, P.; Zimowski, S.; Klimczyk, P.; Dziwisz, T.; Jaworska, L. Mechanical and tribological properties of TiC-based composites for ED machining. *Arch. Mater. Sci. Eng.* **2008**, *33*, 83.

(66) Dias, M.; Guerreiro, F.; Tejado, E.; Correia, J. B.; Mardolcar, U. V.; Coelho, M.; Palacios, T.; Pastor, J. Y.; Carvalho, P. A.; Alves, E. WC-Cu thermal barriers for fusion applications. *Surf. Coatings Technol.* **2018**, *355*, 222.

(67) Jose, S. A.; John, M.; Menezes, P. L. Cermet systems: Synthesis, properties, and applications. *Ceram.* **2022**, *5*, 210.

(68) Casati, R.; Vedani, M. Metal matrix composites reinforced by nano-particles—A review. *Metals* **2014**, *4*, 65.

(69) Malaki, M.; Fadaei Tehrani, A.; Niroumand, B.; Gupta, M. Wettability in Metal Matrix Composites. **2021**, *11*, 1034.

(70) Humenik, M.; Parikh, N. M. Cermets: I, Fundamental concepts related to micro-structure and physical properties of cermet systems. *J. Am. Ceram. Soc.* **1956**, *39*, 60.

(71) Zheng, Y.; Xiong, W.; Liu, W.; Lei, W.; Yuan, Q. Effect of nano addition on the microstructures and mechanical properties of Ti(C, N)-based cermets. *Ceram. Int.* **2005**, *31*, 165.

(72) Córdoba, J. M.; Chicardi, E.; Gotor, F. J. Liquid-phase sintering of Ti(C,N)-based cermets. The effects of binder nature and content on the solubility and wettability of hard ceramic phases. *J. Alloys Comp.* **2013**, *559*, 34.

(73) Malaki, M.; Fadaei Tehrani, A.; Niroumand, B.; Gupta, M. Wettability in metal matrix composites. **2021**, *11*, 1034.

(74) Kubarsepp, J.; Juhani, K.; Tarraste, M. Abrasion and Erosion Resistance of Cermets: A Review. *Mater.* **2021**, *15*, 69.

(75) Gurland, J.; Norton, J. T. Role of the binder phase in cemened tungsten carbide-cobalt alloys. *JOM* **1952**, *4*, 1051.

(76) Manohar, G.; Dey, A.; Pandey, K. M.; Maity, S. R. In *AIP* 2018; Vol. 1952, p 020041.

(77) Sheelwant, A.; Dutta, S.; Sonti, K. S. M.; Narala, S. K. R. Processing and performance assessment of particulate TiB_2 reinforced aluminum MMC developed via a novel hybrid ultrasonic casting system. *Mater. Manuf. Proc.* **2022**, *37*, 186.

(78) Kuo, S.-L.; Chen, Y.-C.; Ger, M.-D.; Hwu, W.-H. Nano-particles dispersion effect on Ni/Al_2O_3 composite coatings. *Mater. Chem. Phys.* **2004**, *86*, 5.

(79) Singh, V. K.; Chauhan, S.; Gope, P. C.; Chaudhary, A. K. Enhancement of Wettability of Aluminum Based Silicon Carbide Reinforced Particulate Metal Matrix Composite. **2015**, *34*.

(80) Manohar, G.; Dey, A.; Pandey, K. M.; Maity, S. R. 2018.

(81) Al-Qureshi, H. A.; Galiotto, A.; Klein, A. N. On the mechanics of cold die compaction for powder metallurgy. **2005**, *166*.

(82) Pörnbacher, J.; Leitner, H.; Angerer, P.; Wojcik, T.; Marsoner, S.; Ressel, G. TiC-(Ti,M)C core-rim structures in solid-state manufactured steel-based MMCs. *Mater. Charact.* **2019**, *156*, 109880.

(83) Johnson, J. L.; Brezovsky, J. J.; German, R. M. Effects of tungsten particle size and copper content on densification of liquid-phase-sintered W-Cu. *Metallurg. Mater. Trans. A* **2005**, *36*, 2807.

(84) Johnson, J. L.; German, R. M. Solid-state contributions to densification during liquid-phase sintering. *Metallurg. Mater. Trans. B* **1996**, *27*, 901.

(85) Gupta, R. K.; Anil Kumar, V.; Khanra, G. P., *Reactive and liquid-phase sintering techniques*, In *Intermetallic Matrix Composites*; Mitra, R., Ed.; Woodhead Publishing: 2018, p 303.

(86) Low, R. J.; Robertson, I. M.; Schaffer, G. B. Excessive porosity after liquid-phase sintering of elemental titanium powder blends. *Scripta Mater.* **2007**, *56*, 895.

(87) Davies, P.; Kellie, J.; Parton, D.; Wood, J. "Metal Matrix Alloys, London and Scandinavian Metallurgical Co Limited," patent application#: WO93/05189, 1993, p 05189.

(88) Tong, X. C.; Fang, H. S. Al-TiC composites In Situ-processed by ingot metallurgy and rapid solidification technology: Part I. Microstructural evolution. *Metallurg. Mater. Trans. A* **1998**, *29*, 875.

(89) Atkinson, H.; Davies, S. Fundamental aspects of hot isostatic pressing: An overview. *Metallurg. Mater. Trans. A* **2000**, *31*, 2981.

(90) Gregg, D. J.; Farzana, R.; Dayal, P.; Holmes, R.; Triani, G. Synroc technology: Perspectives and current status (Review). *J. Am. Ceram. Soc.* **2020**, *103*, 5424.

(91) Munir, Z. A.; Quach, D. V.; Ohyanagi, M. Electric Current Activation of Sintering: A Review of the Pulsed Electric Current Sintering Process. **2011**, *94*.

(92) Munir, Z. A.; Anselmi-Tamburini, U.; Ohyanagi, M. The effect of electric field and pressure on the synthesis and consolidation of materials: A review of the spark plasma sintering method. **2006**, *41*.

(93) Crum, J. V.; Strachan, D.; Rohatgi, A.; Zumhoff, M. Epsilon metal waste form for immobilization of noble metals from used nuclear fuel. *J. Nucl. Mater.* **2013**, *441*, 103.

(94) Chen, X. J.; Khor, K. A.; Chan, S. H.; Yu, L. G. Overcoming the effect of contaminant in solid oxide fuel cell (SOFC) electrolyte: spark plasma sintering (SPS) of 0.5wt.% silica-doped yttria-stabilized zirconia (YSZ). **2004**, *374*.

(95) Bertolino, N.; Garay, J.; Anselmi-Tamburini, U.; Munir, Z. A. Electromigration effects in Al-Au multilayers. *Scripta Mater.* **2001**, *44*, 737.

(96) Nečina, V.; Pabst, W. Comparison of the effect of different alkali halides on the preparation of transparent MgAl2O4 spinel ceramics via spark plasma sintering (SPS). **2020**, *40*.

(97) McCloy, J.; Washton, N.; Gassman, P.; Marcial, J.; Weaver, J.; Kukkadapu, R. Nepheline crystallization in boron-rich alumino-silicate glasses as investigated by multi-nuclear NMR, Raman, & Mössbauer spectroscopies. *J. Non-Cryst. Solids* **2015**, *409*, 149.

(98) Vienna, J. D.; Kroll, J. O.; Hrma, P. R.; Lang, J. B.; Crum, J. V. Submixture model to predict nepheline precipitation in waste glasses. *Int. J. Appl. Glass Sci.* **2017**, *8*, 143.

(99) Parker, W. J.; Jenkins, R. J.; Butler, C. P.; Abbott, G. L. Flash method of determining thermal diffusivity, heat capacity, and thermal conductivity. *J. Appl. Phys.* **1961**, *32*, 1679.

(100) E1461-13(2022), Standard Test Method for Thermal Diffusivity by the Flash Method, ASTM International, West Conshohocken, PA, USA, 2022.

(101) Hay, B.; Filtz, J. R.; Hameury, J.; Rongione, L. Uncertainty of thermal diffusivity measurements by laser flash method. *Int. J. Thermophys.* **2005**, *26*, 1883.

(102) Hammerschmidt, U.; Meier, V. New transient hot-bridge sensor to measure thermal conductivity, thermal diffusivity, and volumetric specific heat. *Int. J. Thermophys.* **2006**, *27*, 840.

(103) Lagüela, S.; Bison, P.; Peron, F.; Romagnoni, P. Thermal conductivity measurements on wood materials with transient plane source technique. *Thermochim. Acta* **2015**, *600*, 45.

(104) Gaiser, J.; Stripf, M.; Henning, F. Enhanced Transient Hot Bridge Method Using a Finite Element Analysis. **2018**, *40*.

(105) Powers, A. *Conductivity in Aggregates*, KAPL-2145, Knolls Atomic Power Laboratory, Schenectady, NY, 1961.

(106) Taylor, R. E.; Bogaard, R. H., *Thermophysical Properties of Dispersion-Strengthened Alloys*, In *Mechanical Properties of Metallic Composites*; Ochiai, S., Ed.; Taylor & Francis Group: 1993, p 59.

(107) De La Rue, R. E.; Tobias, C. W. On the conductivity of dispersions. *J. Electrochem. Soc.* **1959**, *106*, 827.

(108) Maxwell, J. C. *A Treatise on Electricity and Magnetism*; Oxford University Press: London, 1873; Vol. 1.

(109) Rayleigh, L. LVI. On the influence of obstacles arranged in rectangular order upon the properties of a medium. *Phil. Mag J. Sci.* **1892**, *34*, 481.

(110) Yamada, E.; Ota, T. Effective thermal conductivity of dispersed materials. *Wärme Stoffübert* **1980**, *13*, 27.

(111) Miller, J. V. *Estimating Thermal Conductivity of Cermet Fuel Materials for Nuclear Reactor Application*, NASA-TN-D-3898, Lewis Research Center, Cleveland, OH, 1967.

(112) Bruggeman, V. D. Berechnung verschiedener physikalischer Konstanten von heterogenen Substanzen. I. Dielektrizitätskonstanten und Leitfähigkeiten der Mischkörper aus isotropen Substanzen. *Ann. Phys.* **1935**, *416*, 636.

(113) Meredith, R. E.; Tobias, C. W. Conductivities in emulsions. *J. Electrochem. Soc.* **1961**, *108*, 286.

(114) Fricke , H. A Mathematical Treatment of the Electric Conductivity and Capacity of Disperse Systems I. The Electric Conductivity of a Suspension of Homogeneous Spheroids. *Phys. Rev.* **1924**, *24* 575.

(115) Johnson, F. A. *The Thermal Conductivity of Aqueous Thoria Suspensions*, AERE-R/R-2578, United Kingdom Atomic Energy Authority. Research Group. Atomic Energy Research Establishment, Harwell, Berks, England, 1958.

(116) Eucken, A. Allgemeine gesetzmäßigkeiten für das wärmeleitvermögen verschiedener stoffarten und aggregatzustände. *Forsch. Geb. Ingen. A* **1940**, *11*, 6.

(117) Levy, F. A modified Maxwell-Eucken equation for calculating the thermal conductivity of two-component solutions or mixtures. *Int. J. Refridg.* **1981**, *4*, 223.

(118) Kerner, E. The electrical conductivity of composite media. In Proc. Phys. Soc. Sec. B. Vol. 69 p802.

(119) Grossman, L. *Thermal conductivity of coated particle UO_2-Tungsten Cermets*, NASA-CR-1154, General Electric Company for Lewis Research Center, Pleasanton, CA, 1968.

(120) Taylor, R. *Thermal Properties of Tungsten-Uranium Dioxide Mixtures*, AI-64-153 (NASA-CR-54141), Atomics International, Canoga Park, CA, 1964.

(121) Le Flem, M.; Allemand, A.; Urvoy, S.; Cédat, D.; Rey, C. Microstructure and thermal conductivity of Mo–TiC cermets processed by hot isostatic pressing. *J. Nucl. Mater.* **2008**, *380*, 85.

(122) Jubin, R. T.; Aaron, W. S.; Ausmus, C.; Collins, E. D.; de Almeida, V. F.; Del Cul, G.; Johnson, J. A.; Patton, B. D.; Vedder, R. J.; Voit, S. L.; Weber, C. F. Development of Advanced Cermet Waste Forms - 1116. In Proc. 11th Information Exchange Meeting on Actinide and Fission Product Partitioning and Transmutation.

(123) de Almeida, V. F.; Ausmus, C.; Jubin, R. T. Cermet nuclear waste forms: Phase identification and connectivity. *J. Nucl. Mater.* **2022**, *572*, 154082.

(124) Crum, J. V.; Neeway, J. J.; Riley, B. J.; Zhu, Z.; Olszta, M. J.; Tang, M. Dilute condition corrosion behavior of glass-ceramic waste form. *J. Nucl. Mater.* **2016**, *482*, 1.

(125) Chawla, K. K.; Metzger, M. Initial dislocation distributions in tungsten fibre-copper composites. *J. Mater. Sci.* **1972**, *7*, 34.

(126) Chawla, K. K. Thermal cycling of copper matrix-tungsten fiber composites: A metallographic study. *Metallogr.* **1973**, *6*, 155.

(127) Chawla, K. K. *Composite Materials: Science and Engineering*; Springer: New York, NY, 2012.

(128) Molina, J. M.; Narciso, J.; Weber, L.; Mortensen, A.; Louis, E. Thermal conductivity of Al–SiC composites with monomodal and bimodal particle size distribution. *Mater. Sci. Eng. A* **2008**, *480*, 483.

(129) www.matweb.com.

(130) Smith, C. A., *Discontinuous Reinforcements for Metal-Matrix Composites*, In *Composites*; Miracle, D. B., Donaldson, S. L., Eds.; ASM International: 2001; Vol. 21, p 0.

(131) Tatar, C.; Özdemir, N. Investigation of thermal conductivity and microstructure of the α-Al2O3 particulate reinforced aluminum composites (Al/Al2O3-MMC) by powder metallurgy method. **2010**, *405*.

(132) Liu, C. H. Structure and properties of boron carbide with aluminum incorporation. **2000**, *72*.

(133) Yaghobizadeh, O.; Nazari, M.; Mashhadi, M. The effect of rapid microwave sintering process on the electrical conductivity, thermal conductivity and mechanical properties of Al-TiC composites. **2018**, *21*.

(134) Cho, S.; Kim, J.; Lee, J.; Shin, S.; Lee, D.; Kim, M.; Hong, H.-U.; Choi, M.; Lee, Y.-S.; Jo, I.; Lee, S.-K. Phase transformation induced high-strength titanium carbide reinforced stainless steel composites with stable thermo-mechanical properties for high temperature applications. **2022**.

(135) Wilzer, J.; Windmann, M.; Weber, S.; Hill, H.; Bennekom, A. v.; Theisen, W. Thermal conductivity of advanced TiC reinforced metal matrix composites for polymer processing applications. **2015**, *49*.

(136) *Engineered Materials Handbook Desk Edition*; ASM International, 1995.

(137) Fathy, A.; El-Kady, O. Thermal expansion and thermal conductivity characteristics of Cu–Al2O3 nanocomposites. **2013**, *46*.

(138) Sundberg, G.; Paul, P.; Sung, C.; Vasilos, T. Identification and characterization of diffusion barriers for Cu/SiC systems. **2005**, *40*.

(139) Das, S.; Das, S.; Das, K. Synthesis and thermal behavior of Cu/Y2W3O12 composite. **2014**, *40*.

(140) Kida, M.; Weber, L.; Monachon, C.; Mortensen, A. Thermal conductivity and interfacial conductance of AlN particle reinforced metal matrix composites. **2011**, *109*.

(141) Yeo, S.; Baney, R.; Subhash, G.; Tulenko, J. The influence of SiC particle size and volume fraction on the thermal conductivity of spark plasma sintered UO2–SiC composites. **2013**, *442*.

(142) Voigt, W. *Lehrbuch der Kristallphysik*; Teubner, Leipzig: Germany, 1910.

(143) Turner, P. S. Thermal-expansion stresses in reinforced plastics. *J. Res. Nat. Bureau Stds.* **1946**, *37*, RP1745.

(144) Kerner, E. H. The Elastic and Thermo-elastic Properties of Composite Media. *Proc. Phys. Soc. Sec. B* **1956**, *69*, 808.

(145) Miracle, D. B.; Donaldson, S. L., Eds., *ASM Handbook: Composites*, ASM International, 2001.

(146) Riley, B. J.; Rieck, B. T.; McCloy, J. S.; Crum, J. V.; Sundaram, S. K.; Vienna, J. D. Tellurite glass as a waste form for mixed alkali–chloride waste streams: Candidate materials selection and initial testing. **2012**, *424*.

(147) Parruzot, B.; Crum, J. V.; Reiser, J. T.; Neeway, J. J.; Kerisit, S. N.; Daniel, R. C.; Bonnett, J. F.; Reyes, R. A.; Seymour, L. M.; Burns, C. A. Effect of zeolite type, temperature, and pH on Stage III glass alteration behavior for two nuclear waste glasses. *J. Nucl. Mater.* **2022**, *567*, 153717.

(148) C1220-21, Standard Test Method for Static Leaching of Monolithic Waste Forms for Disposal of Radioactive Waste, ASTM International, West Conshohocken, PA, USA, 2021.

(149) C1285-21, Standard Test Methods for Determining Chemical Durability of Nuclear, Hazardous, and Mixed Waste Glasses and Multiphase Glass Ceramics: The Product Consistency Test (PCT), ASTM International, West Conshohocken, PA, USA, 2021.

(150) C1308-21, Standard Test Method for Accelerated Leach Test for Measuring Contaminant Releases From Solidified Waste, ASTM International, West Conshohocken, PA, USA, 2021.

(151) Thorpe, C. L.; Neeway, J. J.; Pearce, C. I.; Hand, R. J.; Fisher, A. J.; Walling, S. A.; Hyatt, N. C.; Kruger, A. A.; Schweiger, M.; Kosson, D. S.; Arendt, C. L.; Marcial, J.; Corkhill, C. L. Forty years of durability assessment of nuclear waste glass by standard methods. *njp Mater. Degrad.* **2021**, *5*, 61.

(152) Shanbhag, V. V.; Yalamoori, N. N.; Karthikeyan, S.; Ramanujam, R.; Venkatesan, K. Fabrication, surface morphology and corrosion investigation of Al 7075-Al_2O_3 matrix composite in sea water and industrial environment. *Proced. Eng.* **2014**, *97*, 607.

(153) Tandler, M.; Sustarsic, B.; Vehovar, L.; Torkar, M. Corrosion of Al/SiC metal-matrix composites. *Mater. Tehnol.* **2000**, *34*, 353.

(154) Vasudevan, N.; Bhaskar, G.; Prasad, A. R.; Suresh, S. Corrosion study on AA5083 aluminum alloy-boron carbide composite. *Mater. Today: Proc.* **2019**, *16*, 1124.

(155) Sherif, E.-S. M.; Almajid, A.; Latif, F. H.; Junaedi, H. Effects of graphite on the corrosion behavior of aluminum-graphite composite in sodium chloride solutions. *Int. J. Electrochem. Sci.* **2011**, *6*, 1085.

(156) Hihara, L.; Kondepudi, P. The galvanic corrosion of SiC monofilament/ZE41 Mg metal-matrix composite in 0.5 M $NaNO_3$. *Corros. Sci.* **1993**, *34*, 1761.

(157) Jaiswal, S.; Kumar, R. M.; Gupta, P.; Kumaraswamy, M.; Roy, P.; Lahiri, D. Mechanical, corrosion and biocompatibility behaviour of Mg-3Zn-HA biodegradable composites for orthopaedic fixture accessories. *J. Mech. Behav. Biomed. Mater.* **2018**, *78*, 442.

(158) Stüpp, C. A.; Mendis, C. L.; Mohedano, M.; Szakács, G.; Gensch, F.; Müller, S.; Feyerabend, F.; Hotza, D.; Fredel, M. C.; Hort, N. Powder metallurgical synthesis of biodegradable Mg-hydroxyapatite composites for biomedical applications. In Proc. Materials Science Forum. Vol. 828 p165.

(159) Stüpp, C. A.; Mendis, C. L.; Mohedano, M.; Szakács, G.; Gensch, F.; Müller, S.; Feyerabend, F.; Hotza, D.; Fredel, M. C.; Hort, N., *Powder metallurgical synthesis of biodegradable Mg-hydroxyapatite composites for biomedical applications*, In *Magnesium Technology*; Manuel, M. V., Singh, A., Alderman, M., Neelameggham, N. R., Eds.; Trans Tech Publ: 2015; Vol. 828, p 165.

(160) Mansfeld, F., *Electrochemical methods of corrosion testing*, In *ASM Handbook - Corrosion: Fundamentals, Testing, and Protection*; Cramer, S. D., Covino Jr., B. S., Eds.; ASM International: 2003; Vol. 13A, p 446.

(161) Scales, C.; Maddrell, E.; Gawthorpe, N.; Begg, B.; Moricca, S.; Day, R.; Stewart, M. Demonstrating a Glass Ceramic route for the Immobilisation of Plutonium containing Wastes and Residues on the Sellafield Site. In Proc. Waste Management 2006. Vol. 6.

(162) Gattu, V.; Asmussen, R.; Tang, M. *Suitability of Cermets as Nuclear Waste Forms: 2023 Cermet Workshop* ANL/CFCT-23/47, Argonne National Laboratory, Lemont, IL, 2023.